Influence of argon ion implantation on the thermoluminescence properties of aluminium oxide

Bokang Khabo

Supervisor: Prof Schadrack Nsengiyumva

Co-Supervisor: Dr Nametso Mongwaketsi

A thesis submitted to the Department of Physics and Electronics, Faculty of Science, Rhodes University, in fulfilment of the requirements for the degree of Master of Science

March 9, 2022

Abstract

The influence of argon ion implantation on the thermoluminescence properties (TL) of aluminium oxide (alumina) was investigated. Aluminium oxide (Al_2O_3) samples were implanted with 80 keV Ar ions. An unimplanted sample and samples implanted at fluences of 1×10^{14}, 5×10^{14}, 1×10^{15}, 5×10^{15}, 1×10^{16} Ar^+/cm^2 were irradiated at a dose of 40 Gy and heated at a rate of 1°C/s using a Risø reader model TL/OSL-DA-20 equipped with a Hoya U-340 filter. The thermoluminescence glow curves showed five distinct peaks with main peaks at 178°C, 188°C, 176°C, 208°C, 216°C and 204°C for the unimplanted sample as well as implanted samples. The peak positions of the samples were independent of the irradiation dose suggesting that the samples were characterised by first order kinetics. This was also confirmed by the T_M-T_{STOP} analysis. It was observed that the TL intensity decreases with fluence of implantation. This observation suggests that the concentration of electron traps responsible for thermoluminescence decreases with ion implantation. The decrease in electron concentration might be due to the formation of non-radiative transition bands or the creation of defect clusters and extended defects following the ion implantation and ion fluence increases. The stopping and range of atoms in matter (SRIM) program was used to correlate the TL response of Al_2O_3 with defects under ion implantation. Subsequent to ion implantation, it was found that the number of oxygen vacancies which are related to electron traps are higher than the number of aluminium vacancies. Kinetic analysis was carried out using the initial rise, Chens peak shape, various heating rate, the whole glow curve, glow curve fitting and the isothermal decay methods. The activation energy was found to be around 0.8 eV and the frequency factor to be of the order 10^8 s^{-1} regardless of the implantation fluence. This means that argon ion implantation did not affect the nature of electron traps. The dosimetric features of samples were also investigated at doses in the range of 40 – 200 Gy. Samples generally showed a superlinear response at doses less than 140 Gy and sublinear response at doses higher than 160 Gy.

Acknowledgements

First and foremost, I would like to express my deepest gratitude to Dr Schadrack Nsengiyumva and Dr Nametso Mongwaketsi for granting me this rare opportunity to conduct my research under their guidance and supervision. Without their hard work, time and dedication this work would have not been completed. May God bless both my supervisors and their families.

I would like to thank iThemba LABS and Dr Mongwaketsi in a special way for securing funding from the NRF for my studies at Rhodes University. Thank you to Dr Mlungisi Nkosi, head of the Tandetron laboratory at iThemba LABS for their assistance and support with top-up funding.

My gratitude to Marc Marteau of the Laboratoire de Physique des matériaux, Université de Poitiers, France for his assistance with ion implantation

To Prof Chithambo the head of the Physics Department I am grateful for the opportunity to use the Labs facilities.

To Dr Mamilola folley I would like to thank you for your assistance in and out of the Lab.

To the staff members and fellow postgraduate students of the Physics Department and Electronics, I would like to thank you for your support and encouragement it meant the world to me. Thank you for making me feel like I belong.

To my mom, I say thank you for all the sacrifices you have made, without you none of this would have been possible.

Contents

Abstract i
Acknowledgements ii
List of Figures v
List of Tables ix
Introduction 1
1.1 Background on ion implantation 1
1.2 Luminescence 3
Ion – Solid Interaction 8
2.1 Ion stopping processes 9
2.1.1 Nuclear stopping 9
2.1.2 Electronic stopping 11
1.3 Ion range parameters 11
2.1.4. Simulation of ion profiles 14
2.2 Radiation damage 15
2.2.1 Collision induced defects 15
2.2.2 Thermally induced defects 16
Thermoluminescence 17
3.1 Theoretical background 17
3.1.1 Mechanism of thermoluminescence 17
3.1.2 Simple model of thermoluminescence 18
3.1.3 Kinetics of thermoluminescence 20
Kinetic analysis methods 22
4.1 Initial rise method 22
4.2 Peak shape method 24
4.3 Various heating rate technique 26
4.4 Whole Glow curve Method 27
4.5 Curve fitting 28
4.6 Isothermal decay method 30
Experimental details 32
5.1 Instrumentation 32
5.1.1 Implantation 32
5.1.2 The Risø TL/OSL luminescence reader 32
Results and discussions 35
6.1 Theoretical investigation on ion impact parameters 35
6.1.1 Ion range 35

6.1.2 Vacancy distribution 37
6.1.3 Energy loss 38
6.2 Thermoluminescence glow curve analysis 39
6.2.1 Assessment of order of kinetics 41
6.2.2 Determination of kinetic parameters 43
6.3 Dosimetric features 58
6.3.1 Dose response of the main peak 59
Conclusions 64
References 66

List of Figures

Figure 1.1: Schematic diagram of an ion implantation system showing the main parts: ion source, ion accelerator, mass separation, beam sweeping and target chamber.

Figure 1.2: Excited state *e* and ground state *g* energy levels showing excitation and emission of fluorescence.

Figure 1.3: Schematic diagram illustrating the process of phosphorescence.

Figure 2.1: An ion incident on crystal lattice is deflected in nuclear collisions with the lattice atoms, and also loses energy in collisions with electrons.

Figure 2.2: A two-dimensional schematic diagram of the path of a single ion that has entered the target at an angle not equal to the surface normal. Note that $R_p = X_s$ only when the incident angle is 0º.

Figure 2.3: Range-energy plot for argon implanted aluminium oxide.

Figure 3.1: A simplified model of the thermoluminescence mechanism: During the excitation stage (a) electrons and holes are produced and are trapped (b) in trapping centers, *Tr*, and recombination centers, *R*. During the heating stage (c) electrons are released to the conduction band and move through the conduction band until they encounter a hole in a recombination center (d). The recombination energy will excite the center and relaxation of the excited center will produce the luminescence.

Figure 4.1: showing the initial rise portion and the critical temperature T_c of a TL glow curve.

Figure 4.2: The geometric shape quantities of a glow curve.

Figure 4.3: Calculation of the area for the whole glow curve method.

Figure 5.1: The Risø TL/OSL Luminescence reader system, model DA-20. (a) The controller unit and (b) the reader unit.

Figure 5.2: A schematic diagram of the reader system. An irradiator is a ^{90}Sr/^{90}Y source; the sample carousel and heater plate are components of the heating system; the light detection system comprises a photomultiplier tube and detection filters.

Figure 6.1: TRIM setup window showing the input parameters used to determine the ion impact parameters.

Figure 6.2: Argon ion profile in Al_2O_3.The implantation energy was 80 keV.

Figure 6.3: Aluminium and oxygen vacancy distribution profiles.

Figure 6.4: Variation of the electronic stopping power and nuclear stopping power as a function of Ar^+ ion beam energy.

Figure 6.5: TL glow curve of the unimplanted Al_2O_3 sample after irradiation to 40 Gy at a heating rate of 1.0ºC/s.

Figure 6.6: TL glow curves of the unimplanted sample and samples implanted at 1×10^{14}, 5×10^{14}, 1×10^{15}, 5×10^{15}, 1×10^{16} Ar+/cm2 after irradiation to 40 Gy at a heating rate of 1.0 ºC/s.

Figure 6.7: TM-TSTOP plot for the unimplanted aluminium oxide (Al_2O_3) sample. The staircase observed is characteristic of first order kinetics.

Figure 6.8: The glow curve of the unimplanted aluminium oxide (Al_2O_3) sample irradiated at different doses and measured at a heating rate of 1°C/s. The inset shows that the main peak is independent of dose.

Figure 6.9. Plots of $ln(I)\ vs\ l/kT$ for the initial rise portion of the main peak of unimplanted sample (a) and implanted samples at fluences: 1×10^{14}(b), 5×10^{14} (c), 1×10^{15}(d), 5×10^{15}(e) and 1×10^{16} Ar^+/cm^2(f).

Figure 6.10: Plots of $ln(T_M^2/\beta)\ vs\ 1/kT_M$ used to determine the activation energy and effective frequency factor for the unimplanted sample (a) and implanted samples at fluences: 1×10^{14}(b), 5×10^{14} (c), 1×10^{15}(d), 5×10^{15}(e) and 1×10^{16} Ar^+/cm^2(f).

Figure 6.11: The effect of various heating rate on the peak temperature for the unimplanted (a) and the sample implanted at the highest fluence of 1×10^{16} Ar^+/cm^2 (b). Both plots show the influence of the various heating rate on the peak intensity (insets).

Figure 6.12: Plots of $ln(I_{Un}/I_{Que}) - 1\ vs\ 1/kT_M$ used to determine the quenching parameters of the main peak of the unimplanted sample (a) and implanted samples at fluences: 1×10^{14}(b), 5×10^{14} (c), 1×10^{15}(d), 5×10^{15}(e) and $1 \times 10^{16}$$Ar^+/cm^2$ (f).

Figure 6.13: Plots of $ln(I/n^b)\ vs\ 1/kT$ for the main peak of the unimplanted sample (a) and implanted samples: 1×10^{14}(b), 5×10^{14} (c), 1×10^{15}(d), 5×10^{15}(e) and 1×10^{16} Ar^+/cm^2 (f). All the samples were irradiated with 40 Gy at 1°C/s.

Figure 6.14: Results from curve fitting of the whole glow peak for the unimplanted sample (a) and implanted samples at fluences 1×10^{14}(b), 5×10^{14} (c), 1×10^{15}(d), 5×10^{15}(e) and 1×10^{16} Ar^+/cm^2(f). All samples were irradiated with 40 Gy at a heating rate of 1°C/s. Open circles are the experimental data and the solid line is the best fit calculated using equation 5.1.

Figure 6.15: Plots of $ln(slope)\ vs\ 1/kT_M$ used to determine the activation energy of the unimplanted (a) and implanted samples at fluences: 1×10^{14}(b), 5×10^{14} (c), 1×10^{15}(d), 5×10^{15}(e) and 1×10^{16} Ar^+/cm^2(f).

Figure 6.16: The variation of peak intensity with dose with the inset showing a plot of peak temperature vs dose (a) and a plot of the superlinearity index *g(D)* vs dose *D* for the unimplanted sample.

Figure 6.17: The variation of peak intensity with dose the inset showing a plot of peak temperature vs dose (a) and a plot of the super-linearity index *g(D)* vs dose *D* (b) for the sample implanted at 1×10^{14} Ar^+/cm^2.

Figure 6.18: The peak intensity as a function of dose with the inset showing the peak temperature as a function of dose (a)and the superlinearity as a function of dose (b) for the sample implanted at 5×10^{14} Ar^+/cm^2. All measurements were carried out at a heating rate of 1ºC/s.

Figure 6.19: The peak intensity as a function of dose with the inset showing the peak temperature as a function of dose (a)and the superlinearity as a function of dose (b) for the sample implanted at $1 \times 10^{15}$$Ar^+/cm^2$. All measurements carried out at a heating rate of 1°C/s.

Figure 6.20: The peak intensity as a function of dose with the inset showing the peak temperature as a function of dose (a) and the superlinearity as a function of dose (b) for the

sample implanted at $5 \times 10^{15} Ar^{+}/cm^{2}$. All measurements were carried out at a heating rate of 1°C.

Figure 6.21: The peak intensity as a function of dose with the inset showing the peak temperature as a function of dose (a) and the superlinearity as a function of dose (b) for the sample implanted at $1 \times 10^{16} Ar^{+}/cm^{2}$. All measurements were carried out at a heating rate of 1°C.

List of Tables

Table 6.1: The peak temperatures and intensities of the main peaks for the unimplanted sample and samples implanted at 1×10^{14}, 5×10^{14}, 1×10^{15}, 5×10^{15}, 1×10^{16} Ar^{+}/cm^{2}.

Table 6.2: The activation energies and frequency factors of all the samples evaluated from the plots of $ln(I)\ vs\ 1/kT$.

Table 6.3: Activation energies and effective frequency factors obtained from Chen's peak shape method.

Table 6.4: The activation energies calculated using the first order two- heating rates equation.

Table 6.5: The activation energies and effective frequency factors obtained from the plots of $ln(T_M^2/\beta)\ vs\ 1/kT_M$.

Table 6.6: The activation energy W resulting from the thermal quenching of unimplanted and implanted samples.

Table 6.7: The order of kinetics b, the activation energy E, and the effective frequency factor s obtained from the whole glow curve method for the unimplanted and implanted samples.

Table 6.8: Kinetic parameters determined from curve fitting for the main TL peaks of all the samples, the samples were irradiated to 40 Gy.

Table 6.9: The activation energy and frequency factor of the unimplanted sample and implanted samples.

Table 6.10: Summary of the activation energies obtained using initial rise, peak shape, whole glow, curve fitting, various heating rate and isothermal methods.

Table 6.11: Summary of the frequency factors obtained using the whole glow, curve fitting, various heating rate and isothermal, initial rise and peak shape methods.

Table 6.12: Summary of the order of kinetics obtained using the whole glow curve and the glow curve fitting methods.

Chapter 1

Introduction

1.1 Background on ion implantation

The control of surface properties is of paramount importance for a wide range of materials in modern technology applications. Over so many years, scientists have been battling with problems related to corrosion, surface hardness, friction, electrical and optical behavior of materials [1].

Techniques such as coating and thermal diffusion have been used to address the above-mentioned challenges. In the semiconductor technology, the thermal diffusion technique was found simple and low cost to introduce dopants into wafers. With the development of ever more complex semiconductor circuitry, with many processing steps and higher densities of components, the limitations of thermal diffusion technology became apparent. One of the limitations of this process is that the doping control is difficult to achieve due to presence of concentration gradients. The addition of ion implantation as an alternative offered the possibilities of low temperature introduction of dopants in semiconductor materials. As a result, modern semiconductor technology has embraced the ion implantation process as a key element in chip production.

Nowadays, ion implantation is a well-established technique, which extends from research laboratory studies of metastable phase formation to production line fabrication of integrated circuits. This widespread application of ion implantation stems from several advantages of this technique: (1) it allows precise control of the total number of implanted ions; (2) it permits independent control of the ion penetration depth; (3) it can use essentially all combinations of ions and target materials; (4) it may achieve concentrations above the equilibrium solid solubility, and above all, (5) it may be used at low or elevated temperatures [1]. An ion implanter in Figure 1.1 consists mainly of an ion source, where ions of the desired element are produced, an ion accelerator where the ions are electrostatically accelerated to a high energy,

a mass separation used for selecting ions with specific mass-to-charge ratio, and a sweeping-and-deflecting device to raster the ion beam across the surface of the material mounted in the target chamber.

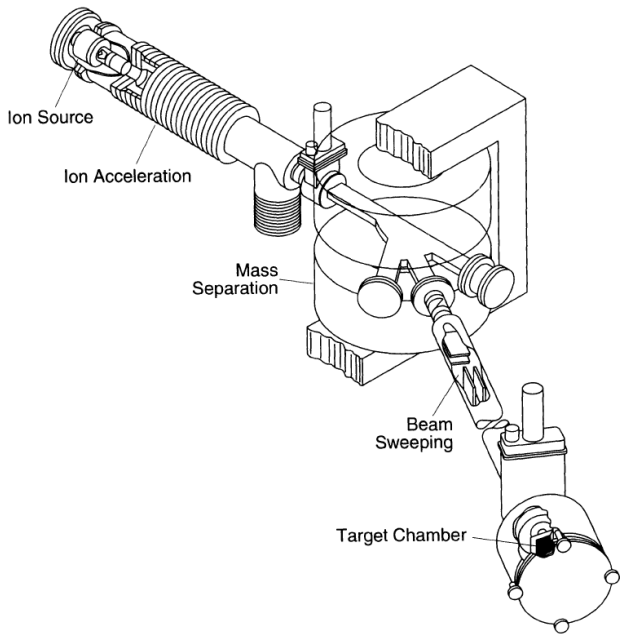

Figure 1.1: Schematic diagram of an ion implantation system showing the main parts: ion source, ion accelerator, mass separation, beam sweeping and target chamber [2]

Apart from the semiconductor technology for improvement of material's electrical properties and the desire to improve the mechanical properties of metals such as wear, friction and hardness, ion implantation has also been used to study insulators to enhance optical properties. The major areas explored so far include [1]:

(1) The reflectivity and refractive index. The focus has been on the index changes to act as anti-reflection coatings, wavelength selective mirrors and bandpass filters, and alterations of properties of coatings and diffused layers.

(2) The lasers for the definition of waveguide laser structures, the impurity addition for lasing regions and definition of harmonic generators by mode matching

(3) The waveguide features for optoelectronics, waveguide parametric amplifiers and production of optically active layers

(4) The luminescence to study colour centre formation, kinetic of defect interactions, phase which results in defects changes, dopant required to control luminescence.

Concerning the latter, ion implantation generates damage which leads to the formation of new defects, and ionization which results in defects in new charge states. Optical methods of studying defects have the advantage that if each defect has characteristic energy levels which lie within the forbidden gap, then they show separable optical absorption and luminescence bands

1.2 Luminescence

Luminescence is the light emitted from irradiated solids, mostly insulators or semiconductors when exposed to ionizing radiation such as beta, alpha, gamma or X-ray irradiation. The ionization frees electrons which then move through the crystal lattice and may be trapped at imperfections within the lattice [3]. Trapped electrons can be thermally or optically released from the trap to recombine with charge carriers of the opposite sign that is, electron-hole recombination. In the recombination processes, the electron relaxes to emit back the absorbed radiation. The relaxation energy is released as light which is the luminescence. For this reason, the emission of light, usually in the visible spectrum, is termed as "luminescence" [4]. Nonradiative recombination may also be possible when the absorbed energy is released as thermal vibration of the lattice or phonons.

There are different forms of luminescence and any type of luminescence requires some input of energy to cause the light emission. All these varieties are distinguished by the source of energy. These include:

1.2.1 Photoluminescence whereby the energy source is the absorption of electromagnetic radiation (photons). This form of luminescence includes fluorescence and phosphorescence.

Fluorescence is luminescence phenomenon where the light is emitted at a time τ less than 10^{-8} seconds after the absorption of radiation. Fluorescence emission is seen to be spontaneous as it has short lifetime. Fluorescence emission is seen to occur simultaneously with absorption of radiation and stops immediately when the radiation ceases. It is essentially temperature independent. Figure 1.2 shows the case of fluorescence in which the absorption of energy causes electrons to move from the

ground state *g* to the excited state *e* shown by transition (i). The inverse path illustrated by transition (ii), that takes place in short time intervals of less than 10^{-8} seconds, is the allowed luminescence transition.

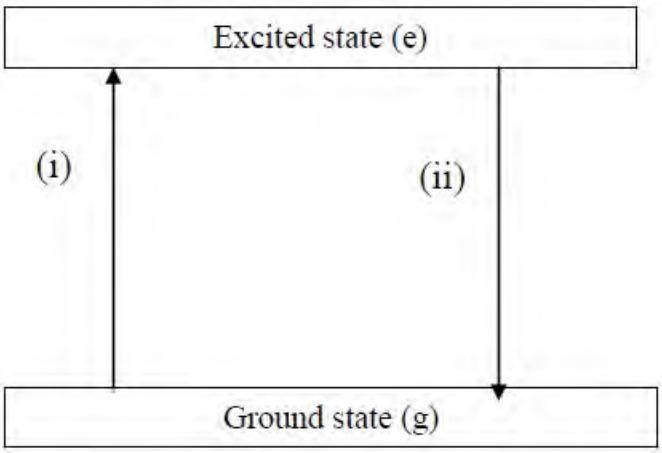

Figure 1.2: Excited state e and ground state g energy levels showing excitation and emission of fluorescence [3].

In phosphorescence, the light is emitted at a time τ greater than 10^{-8} seconds after excitation and the decay of phosphorescence exhibits strong temperature dependence. Phosphorescence is characterized by delay between radiation absorption and light emission. This delay is due to the situation when an electron is excited (e.g., by ionising radiation) from a ground state *g* to a metastable state *m* (electron trap). An electron in the *m*-state can return to the ground state only by passing through the excited state *e* and this transition requires the energy *E*, termed activation energy which can be supplied by heating the sample. The *m*-*e* transition is followed by *e*-*g* transition, which occurs with emission of light as shown in Figure 1.3

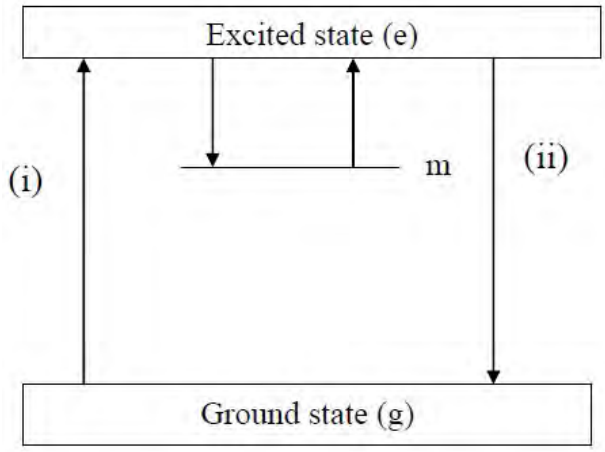

Figure 1.3: Schematic diagram illustrating the process of phosphorescence [3]

Phosphorescence is also classified into two sub-classes: short period phosphorescence where τ is less than or equal to 10^{-4} seconds and long period phosphorescence where τ is greater than 10^{-4} seconds. It is in this long subclass that thermoluminescence is included.

1.2.2 Chemiluminescence. The energy source is a chemical reaction. This includes bioluminescence that involves biochemical reactions in living organisms (like fireflies) and electrochemiluminescence resulting from electrochemical reactions.

1.2.3 Crystalloluminescence. The energy source is crystallisation, the process in which solid crystals precipitate from a solution, a melt or more rarely deposited directly from a gas.

1.2.4 Electroluminescence. The energy source is the electric current passing through the substance. This includes cathodoluminescence resulting from electrons striking a luminescent material.

1.2.5 Mechanoluminescence. The energy source is the mechanical energy on a solid. It includes triboluminescence generated when bonds in a material are broken as the material is scratched or rubbed, fractoluminescence generated when bonds in certain broken by fractures, piezoluminescence produced by the action of pressure on certain solids and sonoluminescence generated by imploding bubbles in a liquid when excited by sound.

1.2.6 Radioluminescence. The energy source is the bombardment by ionising radiation such as β-rays, α-particles, X-rays and γ-rays.

1.2.7 Thermoluminescence. The light emission is caused by moderate heating of a solid, previously exposed to ionizing radiation.

1.3 Aims and objectives

This work aimed at investigating the effects of argon implantation on thermoluminescence properties of aluminium oxide (Al_2O_3). The emphasis of this work was put on the study of the physical processes of luminescence from alumina in order to produce comprehensive knowledge about defects involved in the production of luminescence signal. To achieve this goal, samples of synthetic Al_2O_3 were implanted with 80 keV argon ions at fluences in the range 1×10^{14} – 1×10^{16} ions/cm^2. Thermoluminescence measurements were made at 1 °C/s subsequent to irradiation to 40 Gy.

The objectives of this work were to:

(i) use the Monte Carlo simulation computer code (SRIM) to correlate the thermoluminescence properties of Al_2O_3 with the defect's formation under argon ion implantation and determine ion impact parameters.

(ii) carry out kinetic analysis to determine kinetic parameters including activation energy, frequency factor and order of kinetics for both unimplanted and implanted samples. The methods used to evaluate the kinetic parameters include initial rise, peak shape, various heating rate, whole glow, curve fitting and isothermal decay methods.

(iii) determine the dosimetric features of the investigated samples

1.4 Thesis outline

This thesis is divided into 7 chapters. The introduction which includes the background of ion implantation, the discussion on the various types of luminescence are presented in Chapter 1. Chapter 2 describes the fundamental aspects of ion-solid interactions. Chapter 3 presents the theoretical background of thermoluminescence and the simple model leading to it. The kinetic analysis methods are discussed in Chapter 4. Chapter 5 is dedicated to experimental details. Chapter 6 presents and discusses the results and lastly Chapter 7 summarises the conclusions of this work.

Chapter 2

Ion – Solid Interaction

The advantage of using ion beams is due to their ability to penetrate inside a sample where the knowledge of the interactions between the accelerated ions and target material is used in many different ways in modern research and technology [5 - 7]. Ion beam modification of materials is generally a complex, non-equilibrium thermodynamic process involving both changes of the strain, microstructure and composition in the near surface region [8]. Material properties can be altered depending on the ion fluence, implantation energy, implanted species, target material and temperature.

Typically, implantation starts at energies as low as around 10 eV and may exceed MeV energies. The implanted ions have an approximately Gaussian distribution that is peaked at the mean range beneath the surface that scales with implantation energy, the exact distribution being a function of the fluence and the stopping power of the target [9, 10]. Since the penetration depth of ions from most accelerators is limited to a few microns, only near-surface properties can be controlled independently of bulk phenomena. Practical applications of ion implantation have been used over years in the semiconductor industry [11], where only small implanted concentrations (10^{11} – 10^{14} cm^{-2}) are needed to produce the desired changes in electronic properties. Significantly larger doses (10^{15} – 10^{18} cm^{-2}) are required to alter most properties of interest in metals [12]. In the latter area, ion implantation is used as powerful tool for fundamental research and as a technique for changing metallic surface properties of materials to improve corrosion resistance, wear, friction and hardness [13]. For insulators, the relationship between ion implantation and luminescence has been reviewed. Luminescence has been shown to be an important technique in the study of ion implanted layers and implantation mechanisms and the value of implantation fluence in producing luminescence centres [14]. A proper understanding of the interactions between energetic ions and materials, especially the forces that slow down the ions is therefore important, not only in controlling the depth profile but also in determining the nature of the lattice disorder produced during ion implantation.

2.1 Ion stopping processes

Once a beam of energetic ions is directed onto the surface of a solid, the fast projectiles interact with the stationary near-surface atoms of the solid. In contrast to the interaction of lighter particles, *e.g*. electrons, or photons with matter, the main peculiarity of energetic ion impact is the extremely high localized density of the energy transferred to the target by the ion [15].

As an ion penetrates a solid, it undergoes a succession of binary collisions with target atoms and surrounding electrons, losing energy at each encounter. The energy deposition commonly described by the stopping power, also referred to as the stopping force by some authors [16, 17, 18] gives the energy transfer per path length of a particle along its trajectory. The stopping power is the sum of two independent processes, namely nuclear collisions and electronic collisions [19].
This can be expressed by:

$$\frac{dE}{dx} = \left(\frac{dE}{dx}\right)_{nuclear} + \left(\frac{dE}{dx}\right)_{electronic}. \tag{2.1}$$

The nuclear stopping is dominant at low energies and the energy lost in this process is called nuclear energy loss. The electronic stopping is dominant at high energies, where the displacement of atoms due to elastic collisions is insignificant [20].

2.1.1 Nuclear stopping

Nuclear collisions can involve large discrete energy losses and significant angular deflection of the trajectory of the ion (Figure 2.1). During nuclear collisions, the incident ions are elastically scattered back out of the surface or target atoms may be ejected from the surface via kinetic energy transfer to the lattice atoms. Incident ions may also undergo nuclear reactions giving rise to the emission of reaction products [20].

Nuclear stopping is due to collisions between the incident ion and lattice atoms, where conservation of energy and momentum apply, unless nuclear reactions or nuclear resonances occur as a result of the encounter [19]. The nuclear interactions lead to transfer of kinetic energy to the knock-on target atoms which might be displaced from their original positions (if the transferred energy exceeds the displacement energy), and thus might initiate the formation of structural defects, *e.g.*, vacancies and interstitials in crystalline materials. The probability of an incident ion with energy E undergoing a scattering event or a collision with a target nucleus, while traversing a thickness dx , is defined as

$$P(E) = N\sigma(E)dx \tag{2.2}$$

This probability represents the total fraction of the target surface area which acts as an effective scattering center to the incident energetic particles. N is the number of target atoms per unit volume and $\sigma(E)$ is the total cross section between an energetic ion of energy E and the target atoms.

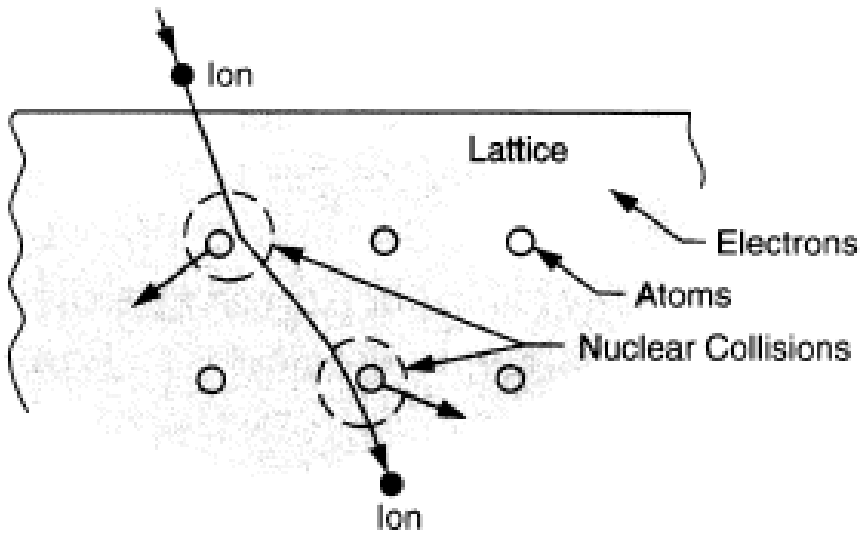

Figure 2.1: An ion incident on crystal lattice is deflected in nuclear collisions with the lattice atoms, and also loses energy in collisions with electrons [21].

2.1.2 Electronic stopping

During electronic collisions, ionization and excitation processes can lead to the emission of radiation in the form of characteristic X-rays [22], optical photons [23, 24], and Auger or secondary electrons [25].

The energy transferred by the ion to the crystal electrons is called electronic stopping or inelastic loss. The large density of electrons and the high frequency of the collisions will contribute to a continuous energy loss during the slowing down of the incident ion. At ion velocities v significantly lower than the Bohr velocity v_0 ($v_0 = \hbar / m_e a_0$) of the atomic electrons, the ion carries its electrons and tends to be neutralized by electron capture. At these velocities, nuclear stopping is dominant [21]. As the ion velocity is increased, the nuclear energy loss diminishes as $1/E_0$, where E_0 is the incident energy of the ion. At higher velocities, the charge state of the ion increases and the maximum stopping power is achieved at around $v > v_0 Z_1^{2/3}$, but the ions are not yet fully stripped. According to Bohr criterion the ions are more than 50 % fully stripped when $v > v_0 Z_1$. At this point, the ion can be viewed as a positive point charge Z_1, moving with a velocity greater than the mean orbital velocity of the electrons in the shells or subshells of the target atom.

1.3 Ion range parameters

One of the most important considerations in any study of ion – solid interactions is the depth (range) distribution of the implanted ions. As mentioned above, the rate at which the projectile loses energy with penetration depth *x* is due to both nuclear and electronic energy-loss terms, as shown in equation (2.1).

The total length R of the penetration of a projectile into a solid can be determined by integrating equation (2.1) to give

$$R = \int_0^{E_0} \frac{dE}{(dE/dx)_n + (dE/dx)_e}, \tag{2.3}$$

where E_0 is the incident energy. As it can be seen in Figure 2.2, R is not the same as the longitudinal projected range (R_p) for a single ion. R_p is the projection of R onto the incident trajectory vector of the single ion. The projected range R_p is commonly defined as the distance measured along the incident ion trajectory at which the highest concentration of implanted ions will be found.

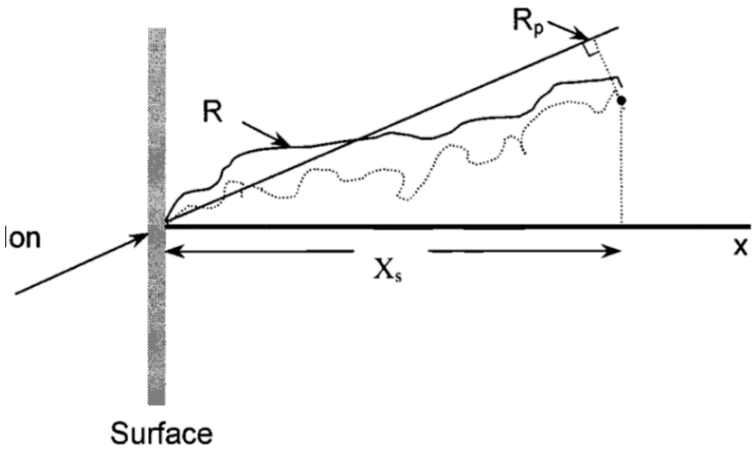

Figure 2.2: A two-dimensional schematic diagram of the path of a single ion that has entered the target at an angle not equal to the surface normal. Note that $R_p = X_s$ only when the incident angle is 0 ° [21].

Since the energy of the projectile is lost to the target atoms and electrons in a series of discrete collisions, the energy loss per collision and the total path length will have a statistical spread of their values. This leads to a near Gaussian distribution of stopping distances, which can be comprehensibly evaluated using a model which is based on the Thomas Fermi statistical model, developed by Lindhard et al [26], known as LSS theory.

Since the stopping of an ion is a stochastic process, the distributions of arbitrary parameters can be characterized by their moments. The first moment gives the mean m of a distribution, and a continuous distribution is defined as

$$\mu = \int_{-\infty}^{+\infty} xf(x)dx, \tag{2.4}$$

where $f(x)$ is the probability function for the random variable of interest.

The second moment is the variance of the distribution, and is defined as

$$\sigma^2 = \int_{-\infty}^{+\infty}(x-\mu)^2 f(x)dx. \quad (2.5)$$

The probability function for a Gaussian distribution, is given by

$$f(x) = \frac{1}{\sigma(2\pi)^{1/2}} exp\left[-\frac{1}{2}\left(\frac{x-\mu}{\sigma}\right)^2\right]. \quad (2.6)$$

The depth distribution $n(x)$ of implanted ions, normalized for an ion implantation dose, or fluence ϕ, is given by comparison with equation (2.6) as

$$n(x) = \frac{\phi}{\Delta R_p(2\pi)^{1/2}} exp\left[-\frac{1}{2}\left(\frac{x-R_p}{\Delta R_p}\right)^2\right], \quad (2.7)$$

where R_p and ΔR_p are the projected range, and straggling respectively.

The dose or fluence is related to the ion depth distribution by

$$\phi = \int_{-\infty}^{+\infty} n(x)dx. \quad (2.8)$$

By setting $x = R_p$ in Eq. (2.7), the expression for the peak atomic density n_p is obtained as

$$n_p = \frac{\phi}{\Delta R_p(2\pi)^{1/2}} \approx \frac{0.4\phi}{\Delta R_p}. \quad (2.9)$$

At low doses implantation profiles can be described by a Gaussian distribution with characteristic parameters R_p and ΔR_p. Higher moments such as skewness and kurtosis measuring the asymmetry and the flatness of the distribution respectively are often necessary to describe the non-Gaussian depth distributions, which occur at higher doses. In our study we

will only focus on two moments, i.e., the projected range and straggling since low implantation fluences have been used.

2.1.4. Simulation of ion profiles

Simulation of ion profiles is performed using the SRIM Monte-Carlo program [27], which stands for the stopping and range of ions in matter. This program calculates the stopping and range of ions in matter using a quantum mechanical treatment of individual ion-atom collisions, assuming the projectile to be an ion, and all target species to be atoms. During the collisions, the ion and atom have a screened coulomb collision, including exchange and correlation interactions between the overlapping electron shells. The charge state of the ion within the target is described using the concept of effective charge, which includes a velocity dependent charge state and long-range screening due to the collective electron sea of the target. Most aspects of the energy loss of ions in matter are calculated in SRIM. Range and straggling distributions for any of ion over a very broad range of energies in any elemental target can be calculated by following the individual trajectories for a set of ions with the same initial conditions. Figure 2.3 shows the variation of range, neglecting sputtering, with the implantation energy in the case of argon implanted $Al_2 0_3$.

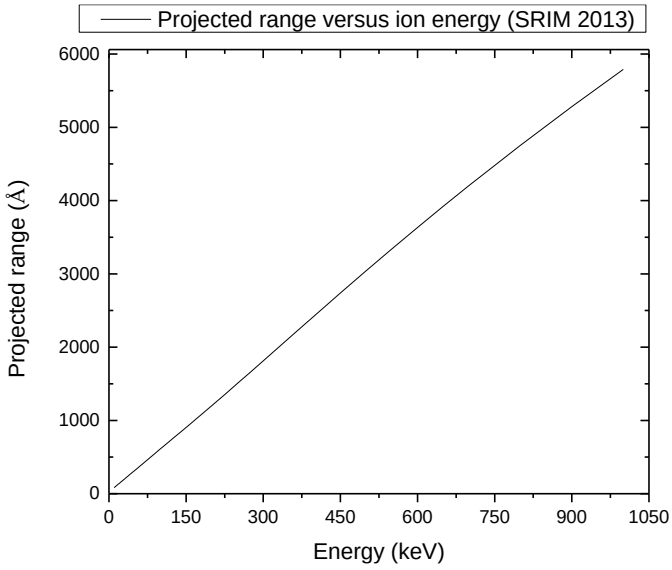

Figure 2.3: Range-energy plot for argon implanted aluminium oxide.

2.2 Radiation damage

The ion implantation process is generally accompanied by radiation damage which is a disorder in the lattice, consecutive to the introduction of energetic ions, ranging from eV to MeV, in the near surface region. In this process, sufficient energy may be transferred from the ion to displace an atom from its equilibrium position. As a result, the recoiling lattice atom can itself displace many other lattice atoms giving rise to a so-called displacement cascade, originating from a single primary collision between the implanted projectile and target atom. This process leads to a distribution of vacancies, interstitial atoms, and other types of lattice disorder in the region around the ion track [28 - 30]. The total amount of damage and its distribution in depth, depend on ion species, ion fluence, ion flux, temperature and energy.

The thickness of the damaged region is expected to be comparable to the projected ion range according to simple theoretical considerations. While this relationship holds for implantation in semiconductors and insulators, in most metals the observed damage region of the crystal lattice extends significantly deeper into the bulk [31, 32].

2.2.1 Collision induced defects

A minimum amount of energy, typically 25 eV [33], is needed to displace an atom from its lattice position. This energy represents the displacement threshold and is called the displacement energy, E_d . If during the collision process the energy transfer T is less than E_d , the struck atom undergoes vibrations with large amplitudes without leaving its lattice site. If, however, $T > E_d$ the struck atom is able to overcome the potential well that represents its stable position. In the simplest situation, the displaced atom leaves a vacancy and occupies an interstitial site in the lattice. This vacancy-interstitial defect is referred to as a Frenkel-defect [30].

The displacement barrier for a lattice atom is not uniform in all directions [21]. Depending on the crystallographic structure, the displacement can be higher or lower than the average. For instance, if the struck atom recoils in a direction where it transfers its kinetic energy to its nearest neighbours, then the displacement barrier will be high and consequently, the

displacement energy to form a Frenkel-defect will also be high. Conversely, in relatively open directions, such as <111> directions, or the <110> directions of a crystal with a *fcc* lattice, the displacement barrier will be low.

2.2.2 Thermally induced defects

As mentioned above, during the slowing down process of energetic ions in a solid, the kinetic energy of a moving ion is partially transferred to host atoms by elastic collisions. The recoiling atoms, in turn, transfer part of their energy to other atoms. All the atomic collisions initiated by a single ion are called a collision cascade. A collision cascade can be divided into three phases [35, 36]. The initial stage referred to as the collisional phase, during which atoms collide strongly and typically lasts about 0.1 – 1 ps. As a result of the collisions, a highly disrupted, very hot (typically 1500 K) region inside the solid is created. The resulting high temperature will spread and be reduced in the solid by heat conduction. This phase is called the thermal spike and lasts roughly 1 ns. When the heat in the thermal spike has dissipated, there will usually be a large quantity of defects in the solid material left. The defects can be of different forms, ranging from point defects to complex interstitial-dislocation loops and volume defects [37,38]. Very low dose implantation results in a number of isolated defects, whose concentration can be estimated from the Kinchin-Pease equation [39],

$$N_v = \frac{F_{Dn}}{E_d}, \tag{2.10}$$

where F_{Dn} is the energy deposited into the sample by atomic collisions, and E_d is the displacement threshold energy. If the local equilibrium lattice temperature during implantation is high enough, many of these defects will relax by thermally activated migration [40]. This phase is referred to as relaxation phase of the collision cascade.

Chapter 3

Thermoluminescence

This chapter discusses the mechanisms of thermoluminescence and the importance of defects in the production of thermoluminescence. To better understand processes which involve transport of charge carriers through the lattice of an insulator or semiconductor, energy band models have been established. These range from a simple model to complex models [3,4,41]. In this chapter we will focus on the simplest model for thermoluminescence as well as the kinetics of thermoluminescence.

3.1 Theoretical background

3.1.1 Mechanism of thermoluminescence

Thermoluminescence (TL) is a phenomenon of emission of light by an insulator or a semiconductor as a result of exposure to ionizing radiations. This phenomenon comes into play when heat is applied to stimulate the release of energy stored during irradiation. The basic effect leading to the production of TL is the trapping of charge carriers, i.e., electrons and holes, produced during exposure to an external source at defect sites in the material.

Many studies including that of Wick et al [42] and Daniels et al [43] have shown that the presence of defects is considered essential for thermoluminescence to occur. Such defects can be divided into two categories: (1) intrinsic defects, i.e., those inherently present in the material such as lattice vacancies and interstitials; (2) extrinsic defects (impurities), i.e., those produced by external means, such as doping or implantation. Defect sites are localized states within the forbidden gap between the valence band and the conduction band whose presence leads to the generation of optical bands that give rise to luminescence.

3.1.2 Simple model of thermoluminescence

The simplest model to describe how materials emit light when heated can be provided by the one trap one recombination center (OTOR) model (Figure 3.1). Absorption of light with energy greater than the band gap results in the ionization of valence electrons, producing energetic electrons and holes which will, after thermalization, produce free electrons in the conduction band and free holes in the valence band. A certain amount of the freed charge carriers will be trapped: the electrons at T_r and the holes at R (transitions). There is a certain probability that the charge carriers escape from these traps due to thermal stimulation. The probability per unit time of release of an electron from the trap, p, is assumed to be described by the Arrhenius equation (3.1).

$$p = s\, exp\left(-\frac{E}{kT}\right). \tag{3.1}$$

The pre-exponential factor s is called the frequency factor or attempt-to-escape-factor. In the simple model, the factor s is considered as a constant (not temperature dependent) with a value in the order of the lattice vibration frequency, namely 10^{12} - 10^{14} s^{-1}.

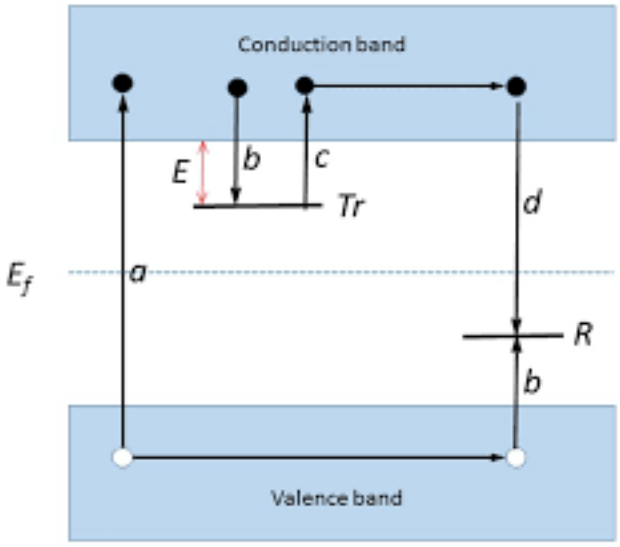

Figure 3.1: A simplified model of the thermoluminescence mechanism: During the excitation stage (a) electrons and holes are produced and are trapped (b) in trapping centers, Tr, and recombination centers, R. During the heating stage (c) electrons are released to the conduction band and move through the conduction band until they encounter a hole in a recombination center (d). The recombination energy will excite the center and relaxation of the excited center will produce the luminescence [44].

E is called the trap depth or activation energy, which is the energy needed to release an electron from the trap into the conduction band, k is the Boltzmann's constant, and T is the absolute temperature. The quantities E and s are called the trap parameters. Their values determine whether the electron will escape at a certain temperature T. If the trap depth $E \gg kT_0$, with T_0 representing the temperature at irradiation, then any electron that becomes trapped will remain so for a long period of time, so that even after exposure to the radiation, there will exist a substantial population of trapped electrons. Furthermore, because the free electrons and holes are created and annihilated in pairs, there must be an equal population of trapped holes at level R. Because the normal equilibrium Fermi level E_f is situated below T_r and above level R, these populations of trapped electrons and holes represent a non-equilibrium state.

By raising the temperature of the TL material above the irradiation temperature, the system returns to the equilibrium state. This increases the probability of detrapping and the trapped electrons will be released from the trap into the conduction band. The charge carrier migrates through the conduction band of the material until it undergoes recombination at recombination center R. In the simple model following Randall and Wilkins [45–47], this recombination center is a luminescent center where the recombination of the electron and hole leaves the center in one of its higher excited states. Return to the ground state is coupled with the emission of light quanta, i.e., thermoluminescence.

However, it should be realized that not every de-excitation leads to the emission of light. The non-radiative transitions depend on the temperature. Sometimes, at higher temperatures, the TL is completely thermally quenched. In the simple model, it is assumed that there is no quenching, i.e., there is no significant decrease of the TL signal and no re-trapping, i.e., all electrons released into the conduction band give rise to recombination under the emission of light. Let us denote n (m^{-3}) as the concentration of trapped electrons and m (m^{-3}) as the concentration of holes trapped at E. Then, the TL intensity $I(t)$, in photons per unit volume and per unit time (m^{-3} s^{-1}) at any time t during heating is proportional to the rate of recombination of holes and electrons at R. This rate of recombination is, under the mentioned assumptions, equal to the rate of thermal excitation of electrons from T_r into the conduction band:

$$I(t) = -\frac{dm}{dt} = -\frac{dn}{dt} = np = ns\ exp\left(-\frac{E}{kT}\right). \tag{3.2}$$

This differential equation (3.2) describes the charge transport in the lattice as a first-order process. Usually, TL is observed as the temperature T is raised as a linear function of time according to:

$$T(t) = T_0 + \beta t \tag{3.3}$$

where β (K s^{-1}) represents a constant heating rate and T_0 the irradiation temperature.

3.1.3 Kinetics of thermoluminescence

3.1.3.1 First order kinetics

The Randall and Wilkins equation 3.2 as reviewed by Chen and McKeever [43] is known as the first-order TL equation. This implies that the rate of electron release is proportional to the initial concentration of trapped electrons. For a first-order peak, the probability of re-trapping is negligible compared to the probability of recombination.

By considering a linear heating rate $\beta = \frac{dT}{dt}$, equation (3.2) becomes

$$\frac{dn}{dT} = -\left(\frac{1}{\beta}\right) ns\ exp\left(-\frac{E}{kT}\right). \tag{3.4}$$

Integration of equation (3.4) leads to

$$I(T) = n_0 s\ exp\left(-\frac{E}{kT}\right) exp\left\{-\frac{s}{\beta}\int_{T_0}^{T} exp\left(-\frac{E}{kT}\right) dT\right\} \quad . \tag{3.5}$$

Equation 3.5 shows TL intensity of first order kinetics. The glow curve displayed by this equation has a characteristic of an asymmetric shape being wider on the lower temperature side [4]

3.1.3.2 Second order kinetics

Garlick and Gibson [48] modified the above view and used the same one trap one recombination center model but included the effects of significant re-trapping of the released charges. This therefore results in the rate of the reaction being proportional to the square of the

trapped charge concentration $dn/dt \propto n^2$ and this is therefore a second order reaction described by

$$\frac{dn}{dt} = -n^2 s' exp\left(-\frac{E}{kT}\right), \tag{3.6}$$

where $s' = s/N$ and N is the total concentration of available electron traps. This results in the Garlick and Gibson equation for TL following second order kinetics,

$$I(T) = \frac{n_0^2 s' exp\left(-\frac{E}{kT}\right)}{\left[1+\frac{n_o s'}{\beta}\int_{T_0}^{T} \exp\left(-\frac{E}{kT}\right)dT\right]^2}. \tag{3.7}$$

The most important feature of this glow curve is that it is almost symmetrical, with the high temperature half of the curve slightly broader than the low temperature half. This is explained by the fact that during the second order reaction, considerable concentrations of released electrons are re-trapped before they recombine, this gives rise to a delay in the TL and spreading out of the emission over a wider temperature range.

3.1.3.3 General order kinetics

The first and second order kinetic equations have been derived with the use of specific assumptions that are related to relative values of re-trapping and recombination probabilities. However, there are cases when these simplified equations do not hold, and the peak does not fit neither the first nor the second order kinetics. May and Partridge [49] derived an empirical expression for general order TL kinetics

$$I(t) = -\frac{dn}{dt} = n^b s' exp\left(-\frac{E}{kT}\right). \tag{3.8}$$

Here *s'* has the dimension of $m^{3(b-1)}s^{-1}$ and *b* is defined as the general-order parameter.

$$I(T) = s'' n_0 exp\left(\frac{-E}{kT}\right) \times \left[1 + (b-10\frac{s''}{\beta}\int_{T_0}^{T} exp\left(-\frac{E}{kT}\right)dT\right]^{-\frac{b}{b-1}}, \tag{3.9}$$

where $s'' = s' n_0^{b-1}$ and has the units s^{-1}. For *b*=2, the general order describes the second order

Chapter 4

Kinetic analysis methods

This chapter presents a brief description of the methods of kinetic analysis used to determine the activation energy *E*, the effective frequency *s* and the order of kinetics *b* for thermoluminescence glow peaks. The methods discussed here are the initial rise, peak shape, various heating rate, whole glow, curve fitting, and isothermal decay methods.

4.1 Initial rise method

The initial rise method is based on the use of the low-temperature interval of a peak under the assumption that the concentration of trapped electrons in the low temperature end of a TL glow peak is approximately constant [48]. In general, the temperature dependence of the TL intensity *I(T)* is given by

$$I(T) = n_0 exp\left[-\frac{E}{kT} - \int_{T_0}^{T} \frac{s}{\beta} exp\left(-\frac{E}{kT}\right) dT\right], \quad (4.1)$$

where *E* is the activation energy of the electron trap, *k* is Boltzmann's constant, β is the heating rate, *T* is the absolute temperature, n_o is the initial concentration of trapped electrons and *s* is the frequency factor and is of the order of the frequency of collisions of the electron with lattice phonons [41].

The number of trapped electrons in the low temperature tail of TL glow peak can be assumed to be approximately constant, since the dependence of *n(T)* on temperature *T* is negligible in that temperature region. Actually, as the temperature increases, the first exponential in equation (4.1) increases while the value of the second term remains close to unity. Based on this assumption, the equation (4.1) reduces to

$$I(T) = Cexp(\frac{E}{kT}), \quad (4.2)$$

where C is a constant including n_o (initial concentration of trapped electrons). Other terms of the equation (4.2) have their usual meaning.

The initial rise method is independent of the order of kinetics and a plot of $ln(I)\ vs\ 1/kT$ is expected to yield a straight line with slope -E. With E known, the frequency factor s can be obtained, in the case of first-order kinetics, from the expression [50]

$$\frac{\beta E}{kT_M^2} = sexp\left(-\frac{E}{kT_M}\right). \tag{4.3}$$

The rule of thumb is that the initial rise portion chosen should not be above 10 - 15% of the peak intensity. This is because the assumption of a constant number of trapped electrons becomes invalid above a critical temperature T_c [51].

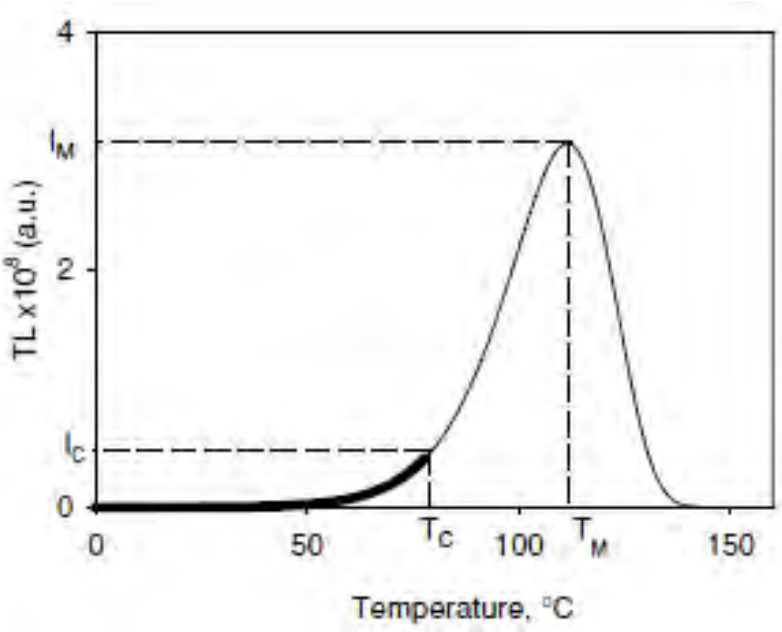

Figure 4.1: The initial rise portion and the critical temperature T_C of a TL glow curve [50].

The initial rise method is appropriate for isolated peaks where the initial rise of the peak being analyzed is not affected by overlapping and nearby peaks. Therefore, it is sometimes necessary to remove secondary peaks to carry out analysis using initial rise method. This can be achieved by a process called thermal cleaning [3]. In this process, the sample is heated beyond the maximum of the first TL peak, is subsequently cooled to a temperature value where the

luminescence is negligible, and then reheated beyond the maximum of the next peak and cooled again. This method should produce clean initial rise curves for each peak. Other considerations when using the initial rise method include making sure there is no temperature lag between the sample and the heating element. The temperature must also be the same throughout the thickness of the sample.

4.2 Peak shape method

This method of kinetic analysis is based on the shape of the glow curve and is used to evaluate the activation energy *E*, the frequency factor *s* and the order of kinetics *b*. Chen [52] suggested an equation that relates trap depth to the total half width $\omega = T_2 - T_1$, the low temperature half width $\tau = T_M - T_1$, the high temperature half width $\delta = T_2 - T_M$.

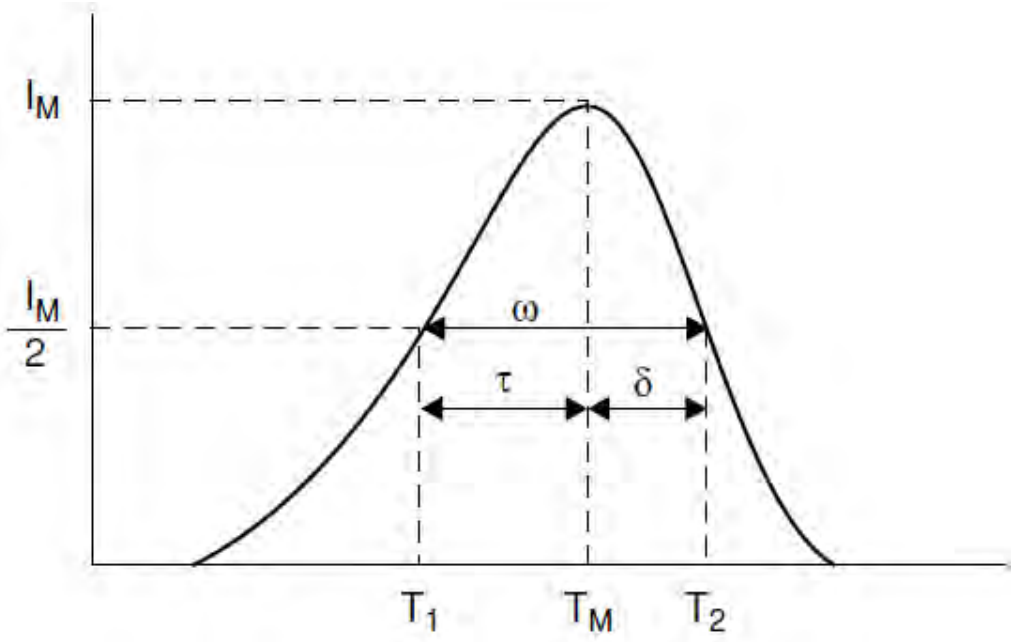

Figure 4.2: The geometric shape quantities of a glow curve [50].

Chen's general equation for activation energy is expressed as

$$E_\alpha = c_\alpha \left(\frac{kT_m^2}{\alpha}\right) - b_\alpha(2kT_M), \tag{4.4}$$

where α can take the values of τ, δ and ω. This method uses Halperin & Braner's [53] geometric factor $\mu_g = \delta/\omega$ to determine order of kinetics b, where $\mu_g = 0.42$ for first order and 0.52 for second order kinetics.

The values for the constants c and b above are as follows:

$$c_\tau = 1.510 + 3.0(\mu - 0.42) \qquad b_\tau = 1.58 + 4.2(\mu - 0.42) \tag{4.5}$$

$$c_\omega = 2.52 + 10.2(\mu - 0.42) \qquad b_\omega = 1 \tag{4.6}$$

$$c_\delta = 0.976 + 7.3(\mu - 0.42) \qquad b_\delta = 0 \tag{4.7}$$

For a first order kinetics, $b = 1$ and $\mu_g = 0.42$, the activation energy equations can be written in the three forms as

$$E_\tau = \frac{1.51kT_M^2}{\tau} - 1.58(2kT_M) \tag{4.8}$$

$$E_\delta = \frac{0.976kT_M^2}{\delta} \tag{4.9}$$

$$E_\omega = \frac{2.52kT_M^2}{\omega} - 2kT_M \tag{4.10}$$

For a second order $b = 2$ and $\mu_g = 0.52$, we get

$$E_\tau = \frac{1.81kT_M^2}{\tau} - 2(2kT_M) \tag{4.11}$$

$$E_\delta = \frac{1.71kT_M^2}{\delta} \tag{4.12}$$

$$E_\omega = \frac{3.54kT_M^2}{\omega} - 2kT_M \tag{4.13}$$

4.3 Various heating rate technique

This method is based on the characteristic shift in peak position T_M as the heating rate is changed. The peak temperature position shifts to higher values when faster heating rates are used. This method is useful in the determination of any order of kinetics as well as calculating kinetic parameters. For first order kinetics the peak temperature T_M can be evaluated by equating the derivative of equation (3.1) to zero

This results in the function

$$\frac{\beta E}{kT_M^2} = sexp\left(-\frac{E}{kT}\right). \tag{4.14}$$

The heating rate can be expressed as

$$\beta = \frac{skT_M}{E} exp\left(-\frac{E}{kT_M}\right). \tag{4.15}$$

From equation (4.15) it is evident that an increase in the heating rate β results in an increase in the peak temperature T_M since the activation energy E and the effective frequency s remain constant. Therefore, the peak temperature increases with heating rate for constant values of E and s.

A method was suggested by Porfianovitch [54] and Booth [55] for calculating E based on two different heating rates for a first order peak. By using two heating rates β_1 and β_2 and their corresponding peak temperatures T_{M1} and T_{M2}, and rearranging equation (4.14) one gets the two-heating rate equation expressed as

$$E = k\frac{T_{M1}T_{M2}}{T_{M1}-T_{M2}} ln\left[\frac{\beta_1}{\beta_2}\left(\frac{T_{M2}}{T_{M1}}\right)\right]^2 \tag{4.16}$$

If the frequency factor s is constant, T_M is dependent on the heating rate β according to the following equation

$$ln\left(\frac{T_m^2}{\beta}\right) = \left(\frac{E}{k}\right)\frac{1}{T_M} + \ln\left(\frac{E}{sk}\right). \tag{4.17}$$

The terms in the equation have their usual meaning.

This means a plot of $ln\,T_M^2/\beta\ vs\ 1/kT_M$ should be linear with slope E and intercept $ln(E/sk)$ [50]. The activation energies were first approximated using the two-heating rate equation (4.16).

4.4 Whole Glow curve Method

This method is based on the measurement of the area under a glow curve *n(T)* from an initial temperature T_0 to a maximum temperature *T*.

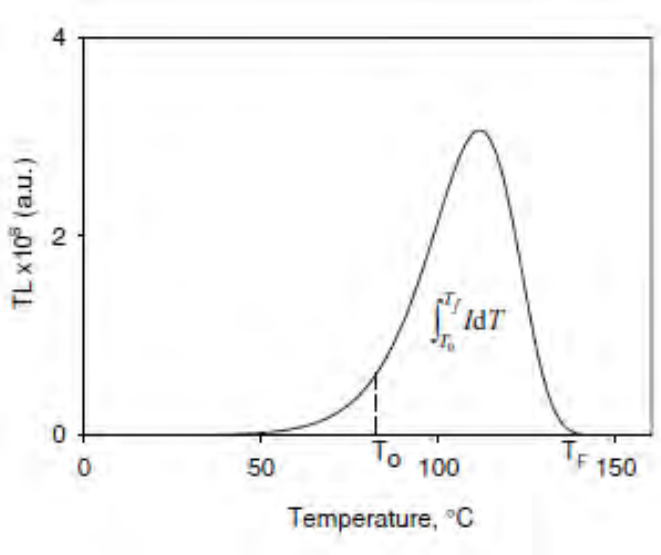

Figure 4.3: The area for the whole glow curve method [50]

The area under the glow peak is expressed as

$$n(T) = \frac{1}{\beta}\sum_{T_0}^{T} I(T)\Delta T \tag{4.18}$$

In terms of the integration,

$$n(T) = \frac{1}{\beta}\int_{T_0}^{T_f} I dT \tag{4.19}$$

Assuming first-order kinetics, and substituting the Randall-Wilkins relation (3.2), leads

$$ln\left[\frac{I}{n(T)}\right] = ln\left(\frac{s}{\beta}\right) - \frac{E}{kT}. \quad (4.20)$$

For a glow peak which follows first order kinetics, $ln\ (I/n(T))\ vs\ 1/kT$ is a linear relationship with slope -*E*, where *E* is the activation energy. From the intercept $ln(s/\beta)$, the frequency *s* can be found.

For general order kinetics the equation (4.3) becomes

$$ln\left(\frac{I(T)}{n^b}\right) = \ln\left(\frac{s'}{\beta}\right) - \frac{E}{kT} \quad (4.21)$$

where *s'* is the effective frequency factor for general order kinetics, β is the heating rate, *n* is the area under the glow peak and *E* is the activation energy [50].
The whole glow curve method can be used to determine kinetic parameters by plotting curves of $ln(I/area^b)\ vs\ 1/kT$. *E* and *s'* are evaluated from the slope and the intercept of the best fit in a graph determined by the value of *b* that yields a straight line with the highest R^2.

4.5 Curve fitting

Curve fitting allows for the analysis of all glow peaks in a multi peak glow curve. The curve fitting process begins by guessing the number of peaks of a glow curve. For first and second order glow peaks, three parameters are involved: the activation energy *E*, the frequency factor *s* and the initial concentration of trapped carriers n_o. For general order kinetics an additional parameter *b* is required.
A glow curve with multiple peaks can be written as

$$I(T) = \sum_{i=1}^{p} \alpha_i f_i(T), \quad (4.22)$$

where α_i is the scaling factor, $f_i(T)$ is the chosen mathematical function for the description of individual glow peaks (first order, second order or general order) and *p* is the number of peaks. If the number of peaks *p* are first order, then 3*p* parameters are involved and 4*p* parameters would be involved for general order [41].

Curve fitting involves guessing parameters, determining $I(T)$ from equation (4.21) and comparing it with the experimental curve. The parameters are then changed until the least difference or residuals between the predicted and experimental data is obtained. Kinetic parameters obtained from other methods are usually used as initial values.
Kitis et al [56] developed equations for first order as

$$I(T) = I_M exp\left[1 + \frac{E}{kT}\frac{T-T_M}{T_M} - \frac{T^2}{T_M^2}\left(1 - \frac{2kT_m}{E}\right) \times \exp\left(\frac{E}{kT}\frac{T-T_M}{T_M}\right) - \frac{2kT_M}{E}\right]. \quad (4.23)$$

For second order

$$I(T) = 4I_M \exp\left(\frac{E}{kT}\frac{T-T_M}{T_M}\right) \times \left[\frac{T^2}{T_M^2}\left(1 - \frac{2kT}{E}\right)\exp\left(\frac{E}{kT}\frac{T-T_M}{T_M}\right)\right].^{-2} \quad (4.24)$$

For general order as

$$I(T) = I_M b^{\frac{b}{b-1}} \exp\left(\frac{E}{kT}\frac{T-T_M}{T_m}\right)\left[1 + (b-1)\frac{2kT_M}{E} + (b-1) \times \left(1 - \frac{2kT}{E}\right)\left(\frac{T^2}{T_M^2}\exp\left(\frac{E}{kT}\frac{T-T_M}{T_M}\right)\right)\right].^{\frac{-b}{b-1}} \quad (4.25)$$

Depending on the number of peaks in a glow curve and the order of kinetics, the theoretical curve *f(T)* will be a combination of equations (4.23) to (4.25). After curve fitting the goodness of fit can be evaluated by the figure of merit (FOM) as suggested by Horowitz and Yossian [57]. The figure of merit is expressed as

$$FOM = \frac{\sum_p |y_{experimental} - y_{fit}|}{\sum_p y_{fit}}. \quad (4.26)$$

Good fit structures have FOM that is less than 3.5%

4.6 Isothermal decay method

The isothermal decay method involves irradiating a sample and quickly heating and holding it at a specific temperature T_i. Thermoluminescence is measured at that temperature for a certain time interval. For first order kinetics the luminescence intensity should decrease according to the exponential function

$$I = I_0 \exp\left(-s \exp\left(\frac{E}{kT_i}\right) t\right). \tag{4.27}$$

A graph of $ln(I)\ vs\ t$ will be linear with the slope of the line being $m_i = -sexp(-\frac{E}{kT_i})$. Taking the natural logarithm gives

$$\ln(\text{slope}) = \ln \text{s} - \frac{E}{kT_i} \tag{4.28}$$

Graphs of the $ln(slope)\ vs\ 1/kT$ should be a straight line with slope -*E* and y-intercept equal to *ln s* [50].

The order of kinetics *b* can also be found by keeping the temperature constant and integrating the general order equation $I(t) = -\frac{dn}{dt} = n^b s' e^{-\frac{E}{kT}}$ to get

$$I(t) = I_0 \left[1 + s' n_0^b \exp\left(-\frac{E}{kT}\right)\right]^{b/(b-1)}, \tag{4.29}$$

where $I_0 = s' n_0^b \exp\left(-\frac{E}{kT}\right)$

Rearranging the above gives

$$\left[\frac{I_t}{I_0}\right]^{\frac{1-b}{b}} = \left[1 + s' \text{t} \exp\left(-\frac{E}{kT}\right)\right]. \tag{4.30}$$

The above equation shows that a plot of $\left[\frac{I_t}{I_0}\right]^{\frac{1-b}{b}} vs\ time$, should be a straight line when a suitable value of *b* is found.

Using different isothermal decay temperatures, a set of straight-line slopes

$m = s' n_0^{b-1}(\mathrm{b}-1)\exp\left(-\frac{E}{kT}\right)$ is obtained and E can be determined from a plot of $ln(m)\ vs\ 1/kT$

b can also be obtained by $ln\left(\frac{dI}{dt}\right) = \ln C + \frac{2b-1}{b}\ln(I)$ plotting $ln\left(\frac{dI}{dt}\right)\ vs\ \ln(I)$ gives a straight line with a slope $m = (2b-1)/b$ from which b can be evaluated by equation (4.30).

Chapter 5

Experimental details

5.1 Instrumentation

5.1.1 Implantation

Aluminium oxide samples of 1mm thickness and 6mm diameter and similar mass (0.100g), supplied by Goodfellow (Cambridge, UK), were used in this study. The samples were implanted with 80 keV argon ions at room temperature using an EATON TM NV 3206 ion implanter at the University of Poitiers, France. Ion fluences were 1×10^{14}, 5×10^{14}, 1×10^{15}, 5×10^{15}, 1×10^{16} Ar^{+}/cm^{2}. The range of argon ions in Al_2O_3 was calculated using TRIM code (SRIM 2008) [27] and estimated to be 507 Å.

5.1.2 The Risø TL/OSL luminescence reader

Thermoluminescence of both unimplanted and implanted samples was measured at Rhodes University, South Africa, using a Risø TL/OSL DA-20 luminescence reader, shown in Figure 5.1. The TL Risø reader is set up into two separate sections: the reader and the controller which contains hardware responsible for the reader's timing, positioning of samples, acquiring data and checking for any errors. The controller also has a display showing the reader's status and the commands being executed and it is connected to a host computer using a RS-232 serial cable or a USB connection.

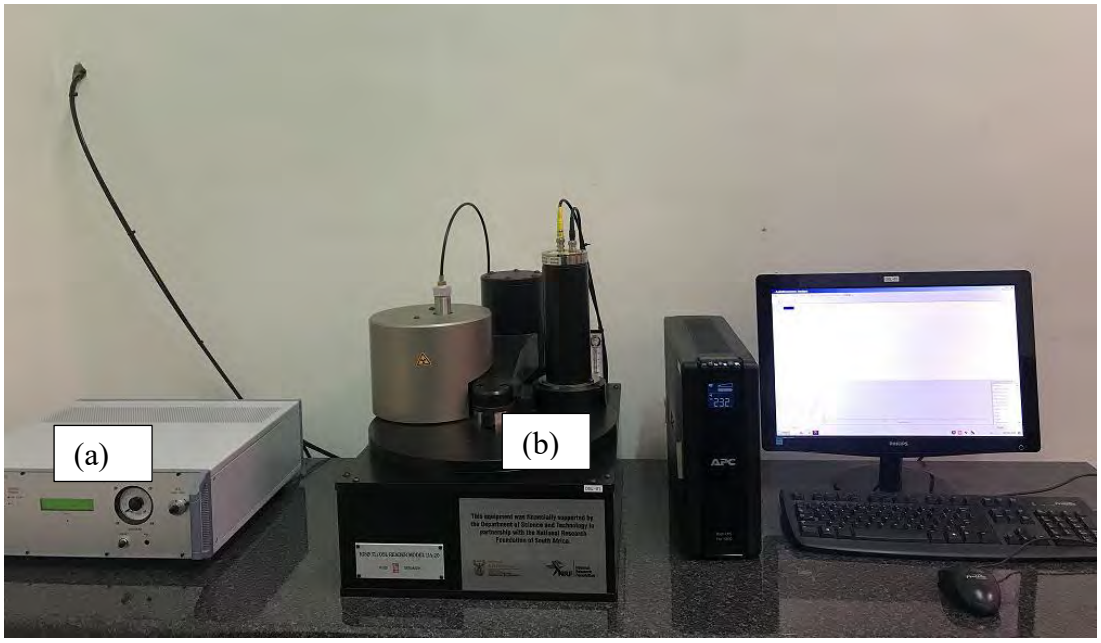

Figure 5.1: The Risø TL/OSL Luminescence reader system, model DA-20. The controller unit (a) and the reader unit (b).

5.1.2.1 The irradiation detection system

The Risø reader model TL/OSL-DA-20 used in this study is equipped with a beta irradiation source. A beta irradiator is located above the sample carousel and it accommodates a $^{90}Sr/^{90}Y$ beta source which has a half-life of 30 years. Beta particles of maximum energy of 2.27 MeV are emitted from the source whose strength is about 1.48 Gbq. The irradiator has a nominal dose rate of 0.1028 Gy/s according to in-house calibration. The irradiation process is software controlled and only single sample irradiation is possible and the minimum irradiation time is 1 second.

5.1.2.2 The luminescence system

The Risø reader model TL/OSL-DA-20 uses two systems of luminescence stimulation [58]. One is the heating system that can be used in TL measurements and the other is a light stimulation system that can be used in OSL measurements. The heating system plays a double role, one is to heat the sample and the second is to lift the sample to the measurement position. Heating is done by feeding a controlled current through the heating element. The heating system is able to heat up to 700 °C at heating rates from 0.1 to 10 K/s. Heating rates above 5 K/s are not usually used in heating because they can cause thermal lag between the sample and the heating system. Nitrogen is used in all measurements of TL to prevent the oxidation of the sample heater and to improve thermal contact between sample holder and heater plate. The

Risø reader model TL/OSL-DA-20 uses also light emitting diodes (LEDs) as light stimulation sources. Two types of LEDs are found in the Risø reader model TL/OSL-DA-20: 21 infrared LEDs (Vishay TSFF 5210) grouped in 3 clusters and 28 blue LEDs (NICHIA type NSPB-500AS) grouped in 4 clusters.

5.1.2.3 The light detection system

The light detection system consists of a photomultiplier tube (PMT) and the detection filters. The PMT is used to detect the emitted luminescence and consists of an input window, a photocathode, focusing electrodes, an electron multiplier and an anode whose role is to provide the signal current that is readout. In Risø TL/OSL reader, the standard PMT is the bialkali EMI 9235QB that has its maximum efficiency ranging between 200 and 400 nm.

The detection filters are used to prevent scattered stimulation light from reaching the PMT. The reader has three main filters namely: the Hoya U-340 (7.5 mm thick, φ = 45 mm), the Schott BG 39 (2 mm thick, φ = 45mm) and the Corning (4 mm thick, φ = 45 mm) &-59 or BG3[1] (3 mm thick, φ = 45 mm), where φ represents the work function of the detector. In this study, the thermoluminescence was detected by an EMI 9235QB photomultiplier tube through a 7 mm Hoya U-340 filter (transmission band 25)

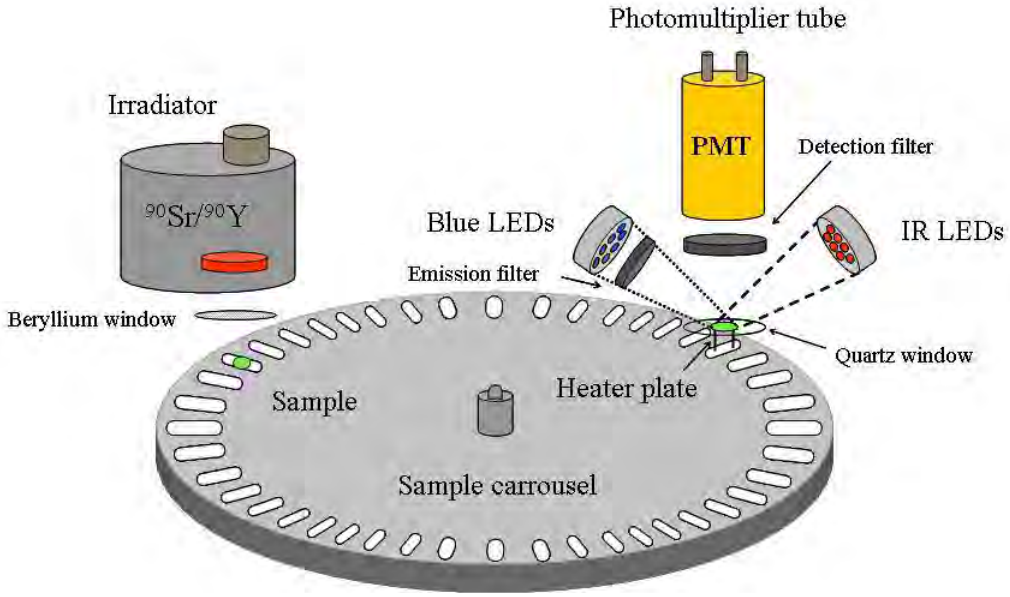

Figure 5.2: A schematic diagram of the reader system [58]. An irradiator is a 90Sr/90Y source; the sample carousel and heater plate are components of the heating system; the light detection system comprises a photomultiplier tube and detection filters

Chapter 6

Results and discussions

In this chapter, the theoretical investigation on ion impact parameters using the Monte Carlo simulation computer code known as Stopping and Range of Ions in Matter (SRIM) is reported in section 6.1. The results obtained from the thermoluminescence (TL) studies carried out on the unimplanted and implanted Al_2O_3 samples are also presented and discussed. The kinetic analysis and dosimetric features will be the main focus in sections 6.2 and 6.3 respectively.

6.1 Theoretical investigation on ion impact parameters

SRIM program is widely used to describe energetic processes of ion-interactions. Its predictive power relies on the accuracy of energy loss/transfer and collisions processes being considered [27]. In this study, SRIM program was used to correlate the TL properties of Al_2O_3 with the defect's formation under argon ion implantation and determine the various ion impact parameters such as range, density, vacancy and energy loss. Prior to the launch of the SRIM program, input parameters including the ion data, the target data, the number of incident ions on the target, the plotting depth and the type of TRIM (SRIM) calculation were set (Figure 6.1). The output files include ion ranges, backscattered ions, transmitted ions/recoils, sputtered atoms and collision events. In this work we are interested in ion range and collision events.

6.1.1 Ion range

Figure 6.2 shows the range profile of the ions that can be characterized by a certain set of parameters that areas the projected range, the straggling, the skewness and kurtosis. The projected range is the average depth of the implanted ions. The straggling value represents the standard deviation in the range of the ions. The skewness tells whether the peak is skewed towards the surface (negative values) or away from the surface (positive values). In other words, a negative skewness indicates that the most probable depth (the peak position) is greater than the mean depth, and positive values indicate the mean depth is greater than the most probable depth. Kurtosis indicates the extent of the distribution tails, with a value of 3.0,

indicating a Gaussian distribution. After simulation, the values for the ion projected range, the straggling, the skewness and the kurtosis were found to be 507 Å, 168 Å, -0.014 and 2.72 respectively. The negative sign of the kurtosis indicates that the peak is slightly skewed towards the surface whereas the value of the kurtosis, 2.72, indicates that the peak follows nearly the Gaussian distribution.

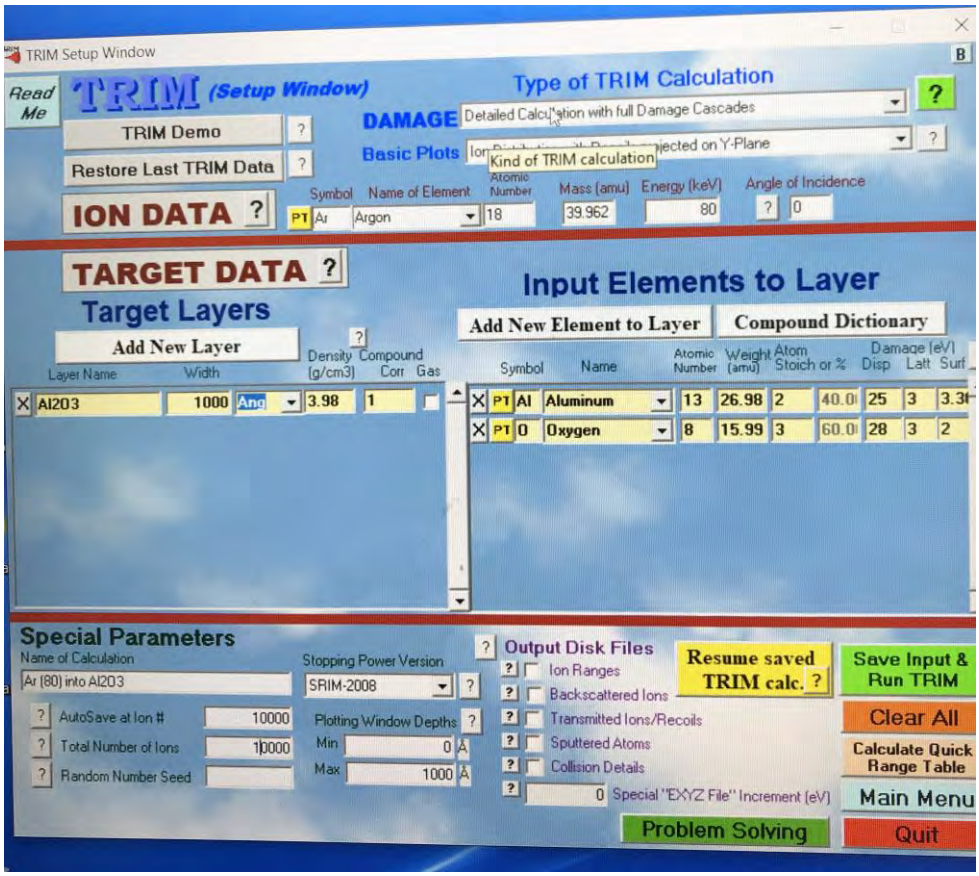

Figure 6.1: TRIM setup window showing the input parameters used to determine the ion impact parameters.

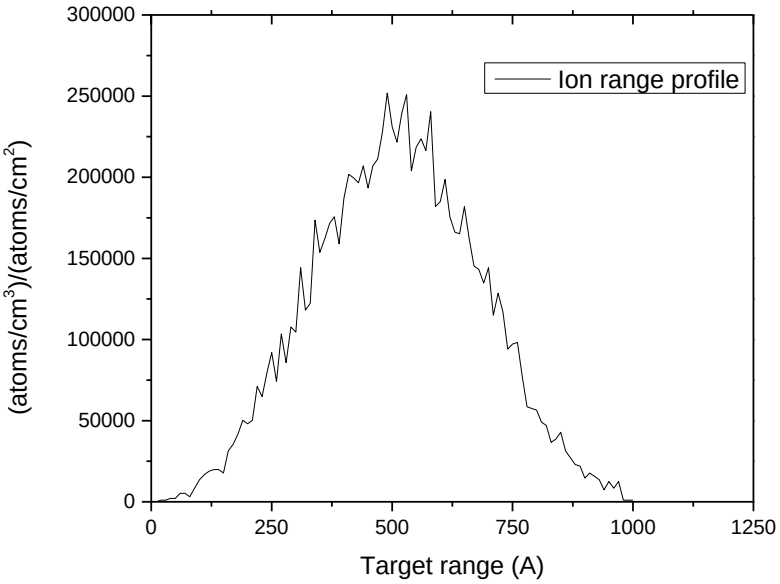

Figure 6.2: Argon ion profile in Al_2O_3. The implantation energy was 80 keV

The ion fluence can be estimated by taking the atomic density of Al_2O_3 found as 2.4 x 10^{22} atoms/cm^3 divided by the ordinate of the plot of ion range versus target depth. The units of the ordinate are (atoms/cm^3)/(atoms/cm^2). The ion fluence was found as 8.0 x 10^{16} atoms/cm^2. This value is nearly in the range of fluences chosen for our implantation process.

6.1.2 Vacancy distribution

Figure 6.3 shows the vacancy distribution profile for Al atoms and O atoms in argon implanted Al_2O_3. The depth for maximum vacancies is 37.5 nm for both Al and O atoms. It can be seen that a good number of vacancies are created after ion implantation. The oxygen vacancies are more than the aluminium vacancies. In Al_2O_3, the oxygen vacancies are related to electron traps. By raising the temperature, these electrons are released from the traps and some of them recombine with holes to give rise to thermoluminescence. Defects induced in aluminium oxide may be of various kinds such as F-centres (oxygen vacancy with two trapped electrons), F^+-centres (oxygen vacancy with one trapped electron), F_2-centres (two linked oxygen vacancies with four trapped electrons), F_2^+-centres (two linked oxygen vacancies with three trapped electrons) and F_2^{2+}-centres (two linked oxygen vacancies with two trapped electrons) [59]

6.1.3 Energy loss

The variation of the electronic stopping power and nuclear stopping power with Ar^+ ion beam energy is shown in Figure 6.4. It shows that at lower energies, the nuclear stopping power is dominant but as the ion energy is increased, the electronic stopping power increases at the expense of the nuclear stopping power. At the value of our implantation energy, i.e, 80 keV, the nuclear stopping power is still greater than the electronic stopping power. This suggests that the damage creation in Al_2O_3 is mainly due to nuclear contribution.

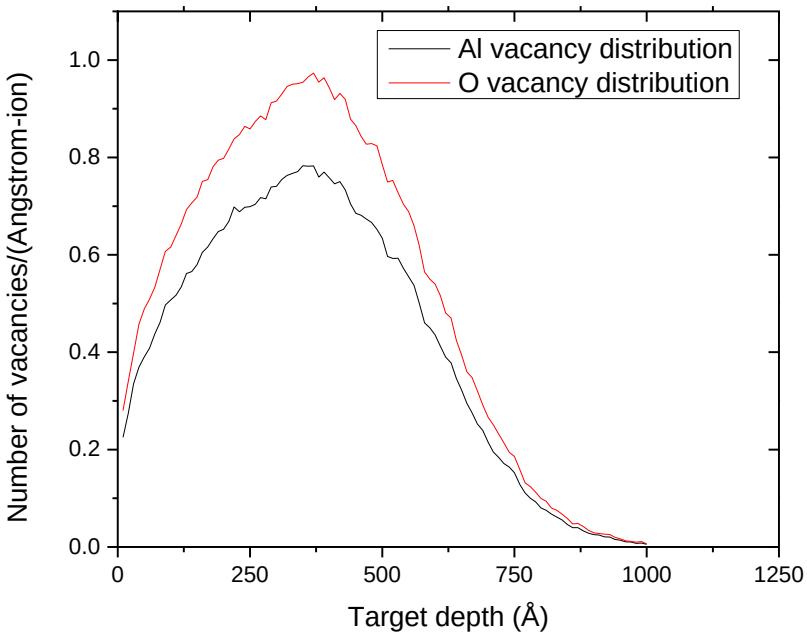

Figure 6.3: Aluminium and oxygen vacancy distribution profiles

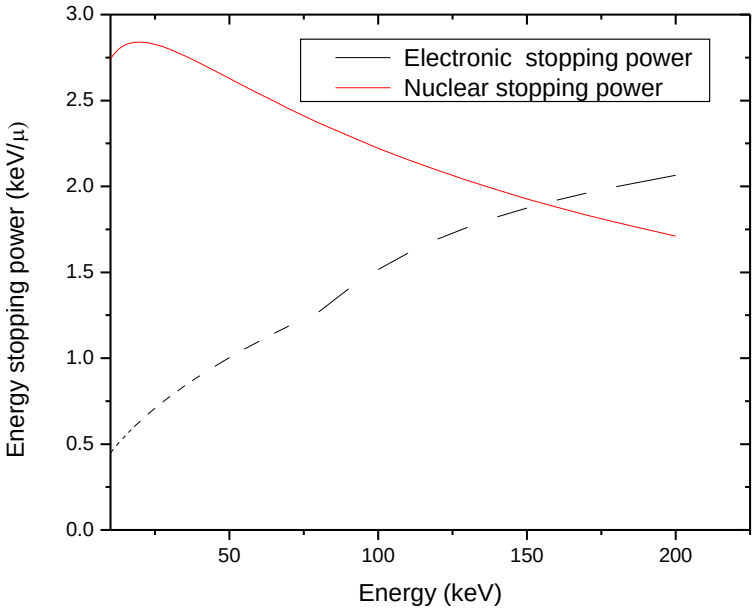

Figure 6.4: Variation of the electronic stopping power and nuclear stopping power as a function of Ar^+ ion beam energy

6.2 Thermoluminescence glow curve analysis

To begin with, the thermoluminescence glow curve of the unimplanted Al_2O_3 sample was measured. The sample was irradiated to 40 Gy and recorded at 1.0 °C/s using a Hoya U-340 filter. The thermoluminescence glow curve is shown in Figure 6.5.

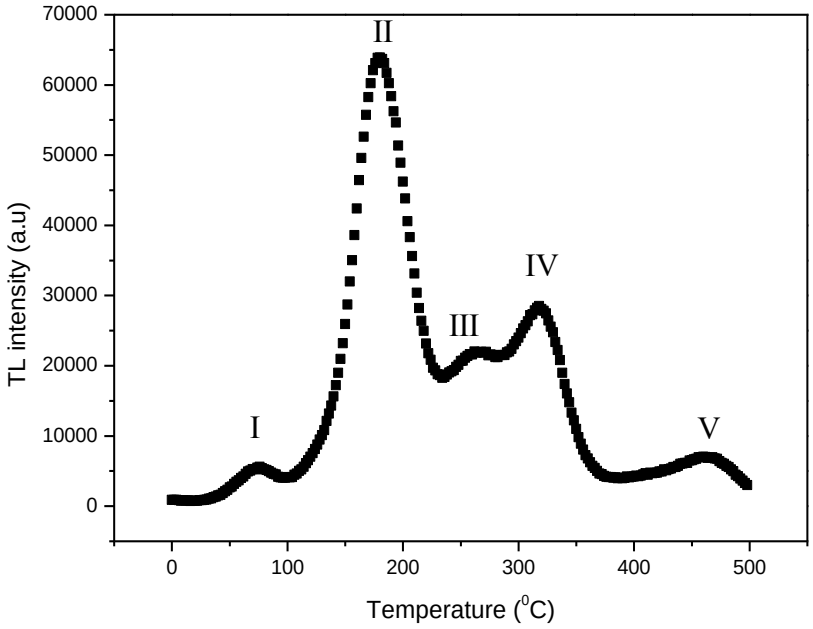

Figure 6.5: TL glow curve of the unimplanted aluminium oxide Al_2O_3 sample after irradiation to 40 Gy at a heating rate of 1.0 ºC/s.

The TL glow curve shown in Figure 6.5 shows five distinct peaks with the main peak at 178°C and secondary peaks at 76°C, 262°C, 318°C and 460°C. The thermoluminescence glow curves of Al_2O_3 samples that were implanted with argon ions at fluences of 1×10^{14}, 5×10^{14}, 1×10^{15}, 5×10^{15} and 1×10^{16} Ar^+/cm^2 were also measured and their glow curves are shown in Figure 6.6. The TL glow curve for the unimplanted sample is included as a reference. Since the focus of this study is on the main peak (peak II), the peak temperature and peak intensity of the main peak for unimplanted as well as implanted samples are shown in Table 6.1. All the samples investigated have the same mass. It can be seen that the intensity of the unimplanted sample is higher than the intensity of the implanted samples.

Table 6.1: The peak temperatures and intensities of the main peak of the unimplanted and implanted samples.

Sample	Peak Temperature (^{0}C)	Peak Intensity (a.u)
Unimplanted	178	63845
1×10^{14}	188	56635
5×10^{14}	176	56035
1×10^{15}	208	53609
5×10^{15}	216	51063
1×10^{16}	204	56695

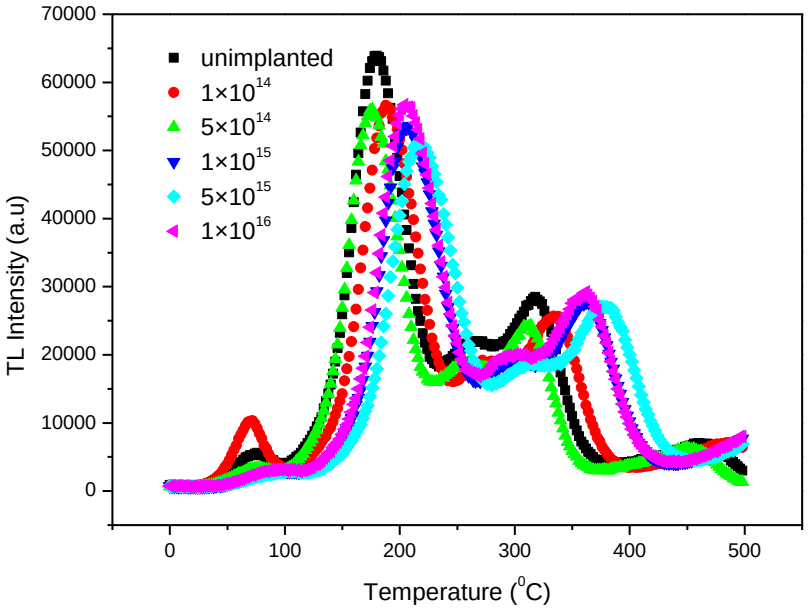

Figure 6.6: TL glow curves of the unimplanted sample and samples implanted at :1×10^{14} , 5×10^{14} , 1×10^{15} , 5×10^{15} , and 1×10^{16} Ar^{+}/cm^{2} after irradiation to 40 Gy at a heating rate of 1.0 ºC/s.

In general, the intensity of the unimplanted Al_2O_3 sample shows the highest intensity. The intensity of the sample decreases with increasing fluence from the lowest fluence of 1×10^{14} to $5 \times 10^{15} Ar^{+}/cm^{2}$ and increases again for the highest fluence of 1×10^{16} Ar^{+}/cm^{2}.
This behaviour was also observed by Nsengiyumva et al and was attributed to the reduction of the trapping centres responsible for thermoluminescence as the implantation fluence was increased [60].

6.2.1 Assessment of order of kinetics

6.2.1.1 T_M-T_{STOP} analysis for the whole glow curve

The order of kinetics was analyzed using the T_M -T_{STOP} analysis [3]. The procedure includes monitoring the position of the thermally stimulated peak as the temperature is increased. First, a previously irradiated sample is heated at a linear rate to a temperature T_{STOP} which corresponds to the low temperature tail of the first glow peak. The sample is then cooled rapidly to room temperature at a similar heating rate and reheated to obtain all the remaining glow curve. The position of the first maximum is recorded. The sample is then irradiated again, and the process is repeated but using a different value of T_{STOP} each time.

In our measurements the unimplanted sample was irradiated to 40 Gy and partially heated to 30°C at a rate of 1°C/s. The sample was then cooled, and the glow curve was measured from room temperature. This procedure was repeated several times on the same sample. The sample was freshly irradiated and the temperature T_{STOP} was increased by 5°C each time until a temperature of 500°C was reached. For each T_{STOP} the position of the T_M was noted and a T_M-T_{STOP} plot was obtained as shown in Figure 6.7.

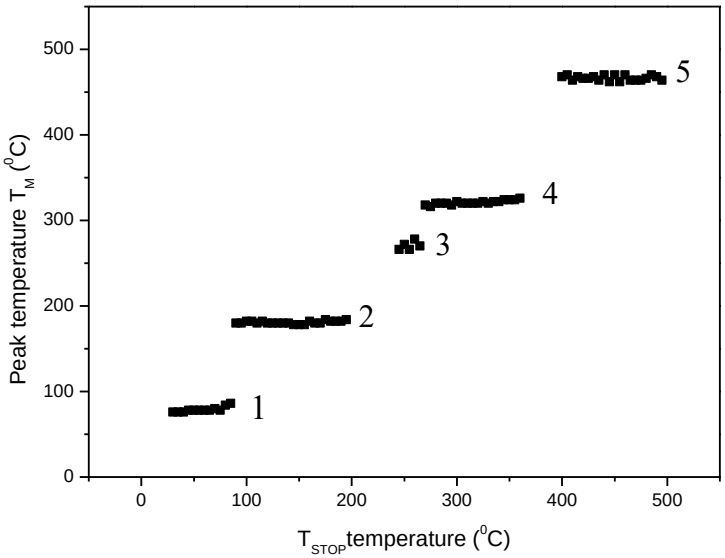

Figure 6.7: T_M-T_{STOP} plot for the unimplanted aluminium oxide (Al_2O_3) sample. The staircase observed is characteristic of first order kinetics [3].

first order kinetics, the position of the glow peak (T_M) is independent of the initial concentration of trapped charges. The T_M is expected to be independent of the T_{STOP} for a first order peak. For second order and closely overlapping peaks, T_M increases with T_{STOP} [50]. The graph of T_M versus T_{STOP} in Figure 6.7 shows a stepwise curve with five flat regions corresponding to five different activation energies. This is consistent with the number of peaks observed from the glow curve. The glow peaks shown in Figure 6.7 follow first order kinetics, including peak 2 representing the main peak.

6.2.1.2 T_M-Dose analysis for the main peak

The T_M-dose analysis was also used to determine the order of kinetics of TL peaks. The sample was irradiated at different doses under similar experimental conditions. For first order peaks, changing irradiation dose does not affect the peak position of the glow peak. For second order

peaks, there is a shift towards lower temperatures as the dose is increased [50]. In our case the unimplanted sample was irradiated from 40 Gy to 200 Gy and the TL intensity was recorded at 1°C/s. Figure 6.8 shows the glow curve of the unimplanted sample irradiated at different doses; the inset shows the peak temperature T_M of the main peak with irradiation dose.

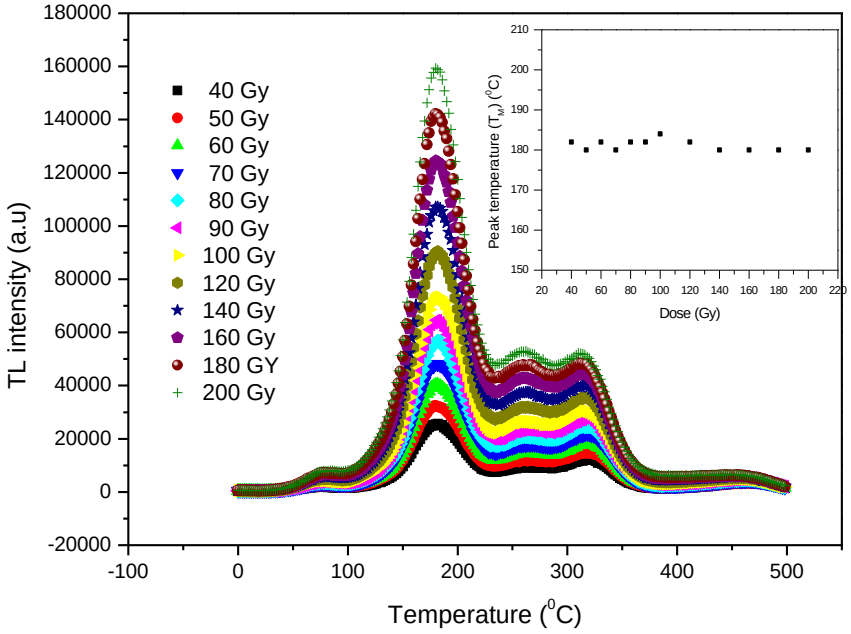

Figure 6.8: The glow curve of the unimplanted aluminium oxide (Al_2O_3) sample irradiated at different doses and measured at a heating rate of 1 °C/s. The inset shows that the main peak is independent of dose.

The peak temperature is stable around 181.2 $\pm$ 1.3 °C with irradiation dose. This confirms that the main peak follows first order kinetics and is in good agreement with the T_M-T_{STOP} analysis.

6.2.2 Determination of kinetic parameters

Kinetic analysis was carried out on the main peak of unimplanted and implanted samples. The peak temperatures and peak intensities are shown in Table 6.1. The methods of kinetic analysis used include the initial rise, peak shape, various heating rate, whole glow curve, glow curve fitting and isothermal decay methods [3,50].

6.2.2.1 Initial rise method

The initial rise method was applied to the glow curves of samples irradiated to 40 Gy at a heating rate of 1°C/s to obtain kinetic parameters. The usual rule of thumb of data between 5 and 15 % of the peak maximum was applied. Plots of $ln(I)\ vs\ 1/kT$ are expected to yield a straight line with slope $-E$. [50]

Because this method is suitable for an isolated peak. A thermal cleaning process was carried out to eliminate the first secondary peak. This was done by preheating the sample to 100 °C which is past the maximum temperature of the first peak and rapidly cooling to room temperature. The sample is then reheated to record the rest of the glow curve. This process removes the secondary peak so that the rising edge of the main peak can be analyzed.

The plots of $ln(I)\ vs\ 1/kT$ for the initial rise portion of the main peak of the unimplanted and samples implanted at fluences of 1×10^{14}, 5×10^{14} ,1×10^{15}, $5\ \times 10^{15}$, 1×10^{16} Ar^{+}/cm^{2} are plotted in Figure 6.9 from (a) to (f) respectively. From the slopes of the plots, the activation energies E were evaluated as shown in Table 6.2 and the frequency factors were calculated using equation (4.3).

Table 6.2: The activation energies and frequency factors of all the samples evaluated from the plots of $ln(I)\ vs\ 1/kT$

Sample	Activation energy E (eV)	Frequency factor s (s^{-1})
Unimplanted	0.68 ± 0.01	1.5×10^{6}
1×10^{14}	0.69 ± 0.01	1.3×10^{6}
5×10^{14}	0.72 ± 0.11	5.0×10^{6}
1×10^{15}	0.73 ± 0.01	1.6×10^{6}
5×10^{15}	0.75 ± 0.01	$1.9\ \times 10^{6}$
1×10^{16}	0.72 ± 0.01	1.4×10^{6}

The activation energy obtained using the initial rise method is about $0.72\ \pm\ 0.02$ eV and the effective frequency is of the order 10^{6}, with no systematic dependency on the fluence of implantation.

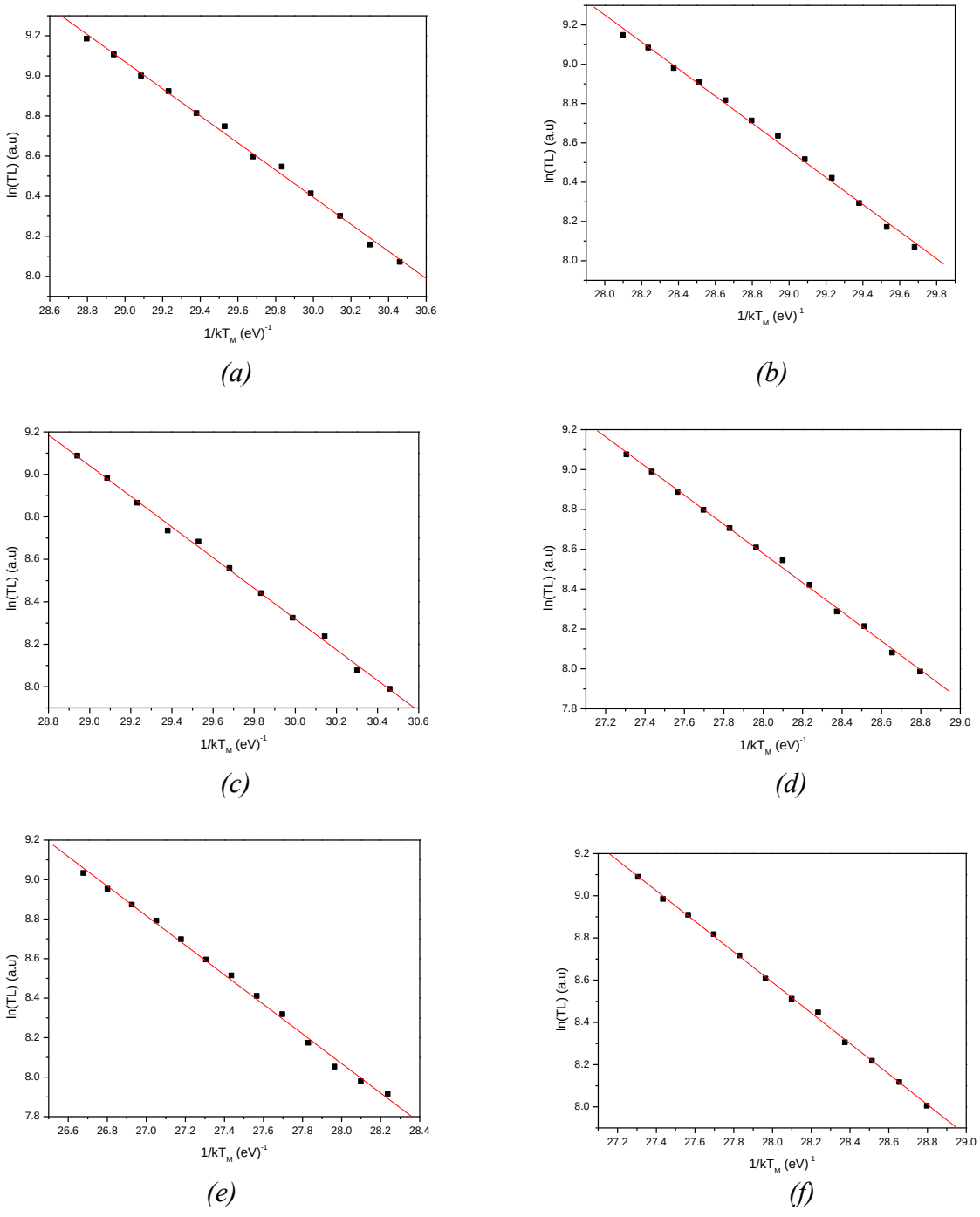

Figure 6.9: Plots of $\ln(I)$ vs $1/kT$ for the initial rise portion of the main peak of unimplanted sample (a) and implanted samples at fluences: 1×10^{14} (b), 5×10^{14} (c), 1×10^{15} (d), 5×10^{15} (e), and 1×10^{16} Ar^{+}/cm^{2}(f).

6.2.2.2 Peak shape method

The peak shape method was used to determine the trapping parameters, that is the activation energy E and the frequency factor s. The peak temperature T_M and peak intensity I_M were determined from the main peak of the unimplanted and implanted samples. The temperatures T_1 and T_2 corresponding to the low temperature and high temperature half maximum intensity were determined. These temperatures were then used to determine τ , ω or δ, where τ is the lower half width and equal to T_M-T_1, δ is the upper half width and equal to T_2-T_M and ω is the half width at half maximum. Activation energies E_τ, E_δ and E_ω were determined using Chen's general equation (4.4).

The kinetic order can be obtained by evaluating its link to the geometric factor $\mu_g = \delta/\omega$ [50]. In particular $\mu_g = 0.42$ for first order and 0.52 for second order kinetics.
Table 6.3 shows the activation energies obtained using Chen's peak shape method using the equation (4.4)

Table 6.3: Activation energies and effective frequency factors obtained from Chen's peak shape method

Sample	E_τ (eV)	E_δ (eV)	E_ω (eV)	Frequency factor s (s^{-1})
Unimplanted	1.22 ± 0.20	1.06 ± 0.19	1.09 ± 0.14	2.3×10^{11}
1×10^{14}	1.07 ± 0.16	1.05 ± 0.20	1.06 ± 0.14	2.2×10^{10}
5×10^{14}	1.22 ± 0.20	1.14 ± 0.22	1.18 ± 0.16	1.2×10^{12}
1×10^{15}	1.19 ± 0.17	1.10 ± 0.18	1.14 ± 0.13	5.4×10^{10}
5×10^{15}	1.03 ± 0.14	1.03 ± 0.17	1.03 ± 0.12	2.1×10^{9}
1×10^{16}	1.19 ± 0.17	1.10 ± 0.18	1.14 ± 0.13	7.0×10^{10}

The average activation energies obtained using Chen's peak shape method were found as: $E_\tau = 1.15 \pm 0.08\ eV$, $E_\delta = 1.08 \pm 0.04\ eV$ and $E_\omega = 1.11 \pm 0.06\ eV$. These values obtained from the different forms of the peak shape method are consistent. The frequency factors corresponding to these activation energies were also determined using the first order kinetics equation (4.3) and were found to be of the order 10^{10}.The values of E and s from the peak shape method are slightly higher than the activation energies and frequency factors obtained from the initial rise method. This discrepancy might due to error made in choosing temperatures corresponding τ, δ and α.

6.2.2.3 Various heating rate method

This method employs the shift in T_M position as the heating rate is changed. The peak temperature shifts to higher values when faster heating rates are used. The various heating rate method was used to determine the activation energy E and the effective frequency s. The samples were irradiated at a beta dose of 40 Gy and TL measurements were carried out at heating rates ranging from 0.2 to 3°C/s.

The activation energy was evaluated using the two-heating rates equation (4.16). Table 6.4 shows the values of the activation energy obtained from the two-heating rates equation. These values depend on the pairs of T_M chosen and therefore can only be used as first estimates.

Table 6.4: The activation energies calculated using the first order two- heating rates equation.

Sample	T_{M1}(K)	T_{M2}(K)	E(eV)	Sample	T_{M1}(K)	T_{M2}(K)	E(eV)
Unimplanted	427	449	1.04	1×10^{15}	445	461	1.14
	427	469	0.83		445	503	0.65
1×10^{14}	433	451	0.95	5×10^{15}	451	473	0.84
	433	483	0.71		451	513	0.62
5×10^{14}	421	437	1.01	1×10^{16}	443	463	0.89
	421	459	0.89		443	503	0.62

The various heating rate method was also used to determine the activation energy. According to equation (4.17), plots of $ln(T_M^2/\beta)\ vs\ 1/kT_M$ should be linear with slope E and intercept ln(E/sk). Figure 6.10 shows plots of $ln(T_M^2/\beta)\ vs\ 1/kT_M$ for the unimplanted and implanted samples all irradiated with 40 Gy at a heating rate of 0.2 - 3°C/s. The activation energies evaluated from these plots are shown together with their effective frequency factors in Table 6.5. The effective frequency factor was calculated from the intercept of equation (4.17).

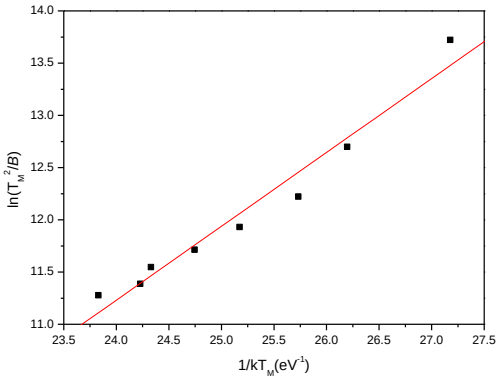

(a)

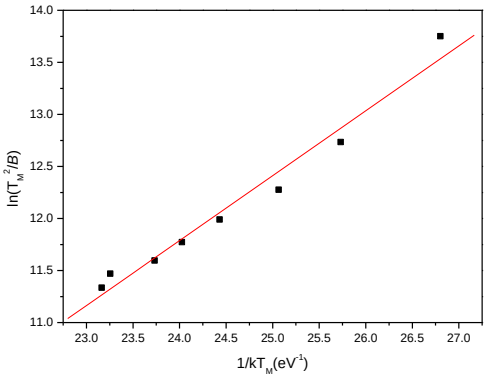

(b)

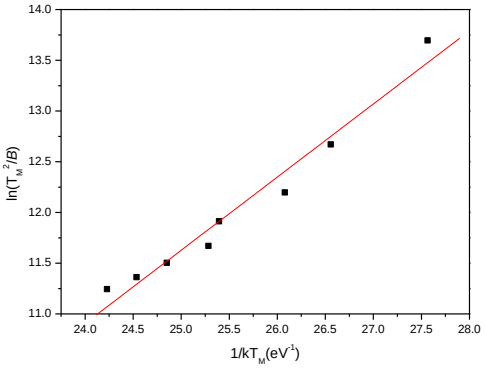

(c)

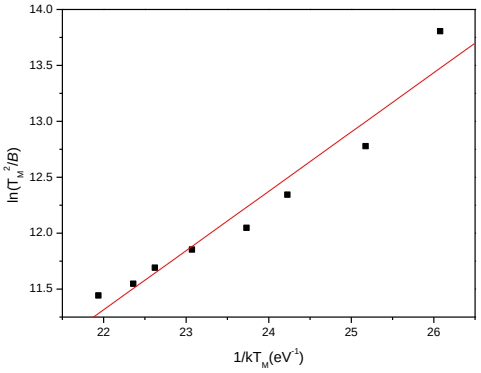

(d)

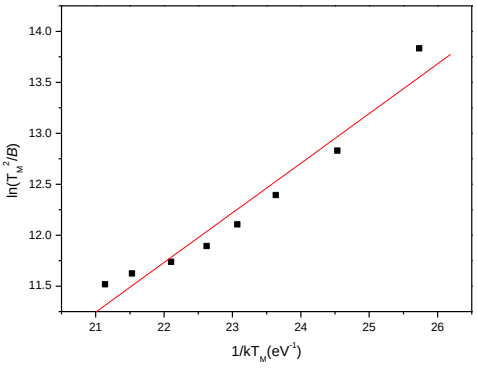

(e)

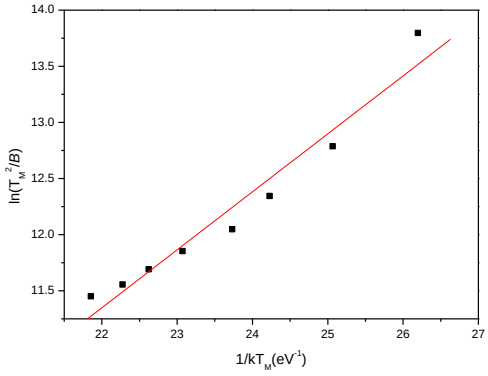

(f)

Figure 6.10: Plots of $\ln(T_M^2/\beta)$ vs 1/kT used to determine the activation energy and effective frequencey factor for the unimplanted sample (a) and implanted samples at fluences: 1×10^{14}(b), 5×10^{14}(c), 1×10^{15}(d), 5×10^{15}(e), and 1×10^{16} Ar^+/cm^2(f).

Table 6.5: The activation energies and effective frequency factors obtained from the plots of $ln(T_M^2/\beta)$ vs $1/kT_M$

Sample	Activation energy E (eV)	Frequency factor (s^{-1})
Unimplanted	0.71 ± 0.06	2.56×10^6
1×10^{14}	0.62 ± 0.04	1.74×10^5
5×10^{14}	0.72 ± 0.05	5.03×10^6
1×10^{15}	0.52 ± 0.05	0.16×10^5
5×10^{15}	0.49 ± 0.05	$0.27.\times 10^5$
1×10^{16}	0.52 ± 0.06	0.11×10^5

Figure 6.11 (a) and (b) shows the effects of the various heating rates on the position of the main TL peak for the unimplanted and the sample implanted at a fluence of $1\times10^{16}Ar^+/cm^2$ respectively. The insets show the influence of the various heating rate on the peak intensity of the samples. From Figure 6.11 (a), it is evident that the peak temperature T_M shifts to higher values as the heating rate is increased and this is true for all the samples investigated.

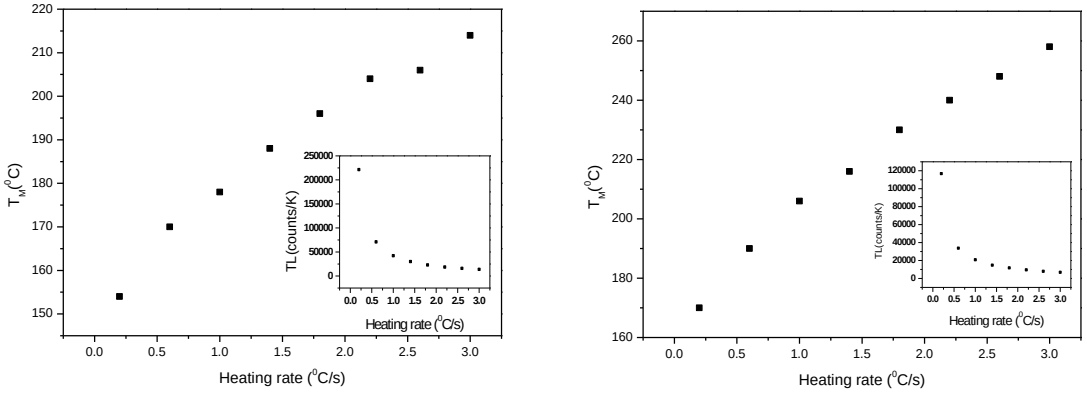

Figure 6.11: The effect of various heating rate on the peak temperature for the unimplanted (a) and the sample implanted at the highest fluence of 1×10^{16} Ar^+/cm^2 (b). Both plots show the influence of the various heating rate on the peak intensity (insets).

The insets show a decrease in intensity with heating rate. This has been observed in all samples investigated. This decrease suggests that the main peak is affected by thermal quenching [50]. A thermal quenching analysis was therefore conducted to determine the activation energy of thermal quenching *W*.

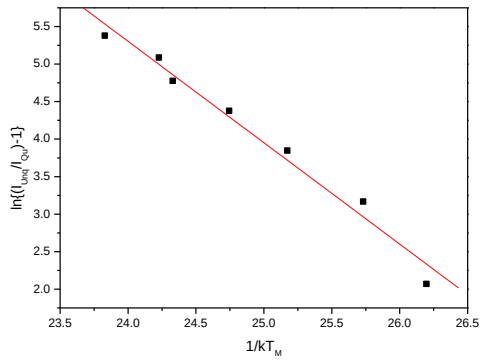

(a)

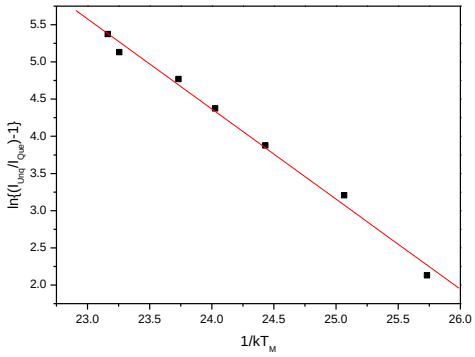

(b)

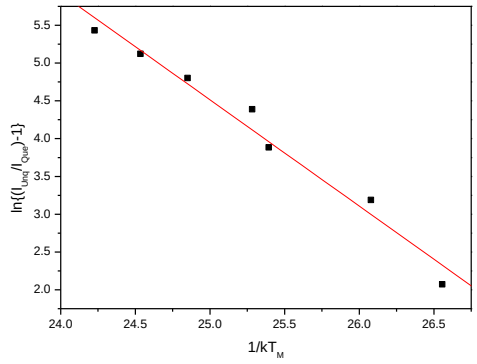

(c)

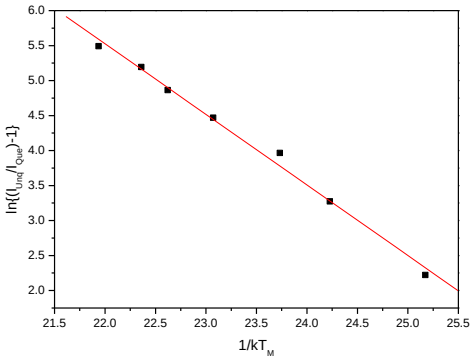

(d)

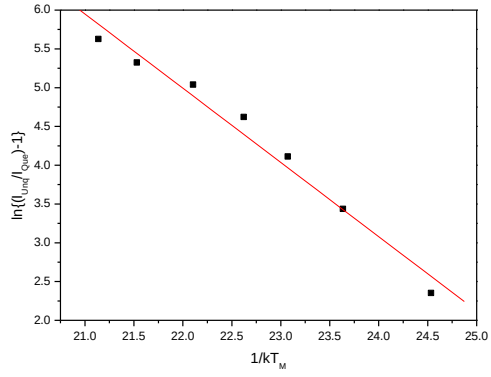

(e)

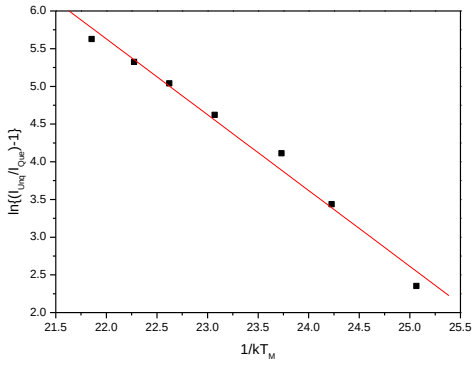

(f)

Figure 6.12: Plots of $\ln(I_{Un}/I_{Que}) - 1$ vs $1/kT_M$ used to determine the quenching parameters of the main peak of the unimplanted sample (a) and implanted samples at fluences: 1×10^{14} (b), 5×10^{14} (c), 1×10^{15}(d), 5×10^{15}(e), and 1×10^{16} Ar^{+}/cm^{2} (f).

The area under the quenched peak (peak integral) I_{Que} is given by $I_{Que} = \eta(T)I_{Un}$, where $\eta(T)$ is the luminescence efficiency and I_{Un} is the unquenched peak integral. $\eta(T)$ is approximated to be equal to $\eta(T_M)$ and is referred to as the quenching efficiency [50].
The quenching efficiency is expressed as

$$\eta(T_M) = \frac{1}{1+Cexp(-W/kT_M)}, \tag{6.1}$$

where *C* is the thermal quenching pre-exponential factor, *W* is the activation energy of thermal quenching and *k* is the Boltzmann's constant. The parameters *C* and *W* can be obtained from a plot of

$$ln\left(\frac{I_{Un}}{I_{Que}}\right) - 1 \; vs 1/kT_M \tag{6.2}$$

Figure 6.12 (a) - (f) shows the plots used to determine the activation energy of thermal quenching of the unimplanted and implanted samples.

Table 6.6: The activation energy W resulting from the thermal quenching of unimplanted and implanted samples.

sample	*W* (eV)
Unimplanted	1.35
1×10^{14}	1.21
5×10^{14}	1.41
1×10^{15}	1.01
5×10^{15}	0.96
1×10^{16}	1.01

The activation energy *E* and the frequency factor *s* of all investigated samples using the various heating rate method were of the order 0.60 ± 0.10 eV and $10^4 \ s^{-1}$ respectively. Compared to other kinetic analysis methods, the various heating rate method gives underestimated values of *E* and *s*. Pagonis et al [61] attribute this to the anomalous heating rate effect involving strong competitions between radiative and non-radiative pathways. As the probability of the non-radiative processes increases, the anomalous heating rate becomes dominant and the various heating rate method could at this level underestimate the values of *E* and *s*. It is also observed that the intensity of the glow peaks decreases with increasing heating rates. This suggests that the glow peaks are affected by thermal quenching. Such a decrease in the luminescence

efficiency is attributed to the increase of non-radiative transitions at recombination centres. The activation energy of thermal quenching W was of the order 1.12 ± 0.20 eV

6.2.2.4 Whole glow peak method

The whole glow method was used to determine the trapping parameters E, s and b for the main peak of all the samples. Curves of $ln(I/area^b)\ vs\ 1/kT$ using different values of b were plotted and values of b that yield a straight line with the highest R^2 were adopted.

For this study values of b from 0.9 to 1.2 were used. Graphs of $ln(I/area^b)\ vs\ 1/kT$ were plotted for the unimplanted sample, samples implanted with fluences of 1×10^{14}, 5×10^{14}, 1×10^{15}, 5×10^{15}, 1×10^{16} Ar^+/cm^2 using ΔT= 2K and β =1 Ks^{-1}. The samples were irradiated to 40 Gy at 1 °C/s.

Table 6.7 shows the order of kinetics and the activation energies obtained from the plots of $ln(I/n^b)\ vs\ 1/kT$. The frequency factor s was evaluated from the y-intercepts of the graph and calculated using equation (4.20)

Table 6.7: The order of kinetics b, the activation energy E, and the effective frequency factor s obtained from the whole glow curve method for the unimplanted and implanted samples.

Sample	Order of kinetics (b)	Activation energy E (eV)	Frequency factor s (s^{-1})
Unimplanted	0.9	0.82 ± 0.02	2.01×10^8
1×10^{14}	0.9	0.85 ± 0,02	3.02×10^8
5×10^{14}	0.9	0.78 ± 0.02	9.15×10^8
1×10^{15}	0.9	0.84 ± 0.02	1.01×10^7
5×10^{15}	0.9	0.87 ± 0.02	1.36×10^8
1×10^{16}	0.9	0.84 ± 0.02	9.45×10^7

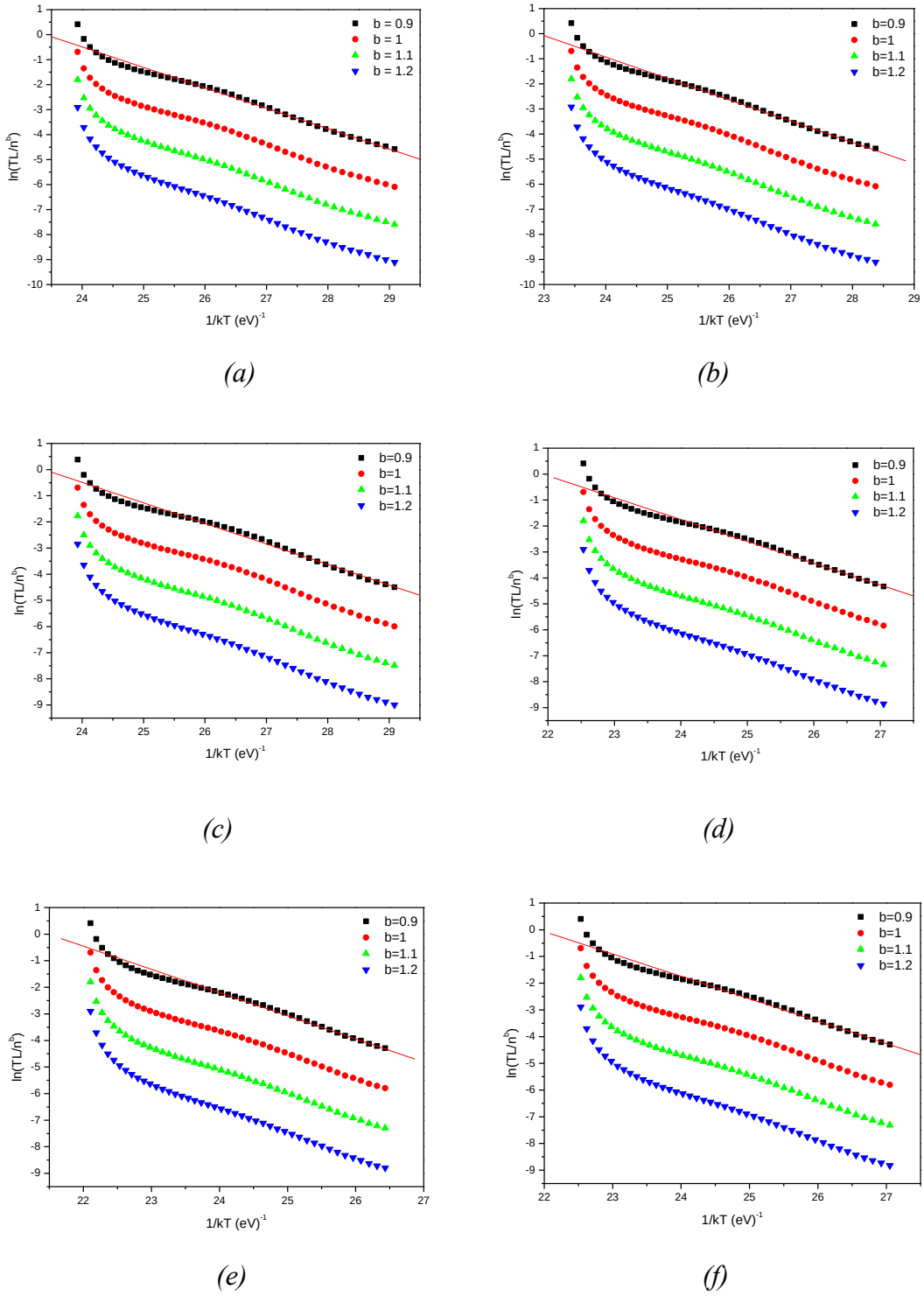

Figure 6.13: Plots of ln(I/n^b) vs 1/kT for the main peak of the unimplanted sample (a) and implanted samples: 1×10^{14} (b), 5×10^{14} (c), 1×10^{15} (d), 5 ×10^{15} (e), and 1×10^{16} Ar^+/cm^2(f). All the samples were irradiated with 40 Gy at 1 °C/s.

The order of kinetics *b* which gave the highest value of R^2 was 0.9. The activation energy was determined to be 0.83 ± 0.03 eV and the frequency factor to be of the order $10^8\ s^{-1}$. The activation energy is in good agreement with that found using Chen's peak shape method.

6.2.2.5 Glow curve fitting

Curve fitting was used to determine a set of parameters which results in the least difference or residuals between the predicted and experimental data. The general order equation was used together with the sigma plot fit curve command software to fit the whole glow curve to determine unknown parameters. This method relies on two measured quantities being the maximum TL intensity and the temperature corresponding to that maximum temperature T_M [50].

Peak resolution methods used in section 6.2.1 revealed that the glow curves consisted of five peaks. However, analysis was carried out on glow curves where the first secondary peak was thermally cleaned. Therefore, the equation used for the curve fitting was a sum of the four terms given by the general-order TL equation (4.25).

In curve fitting the appropriate values of *E* and *b* are those that give the best fit between the data and the model after iteration. The results of the activation energy *E*, frequency factor *s*, order of kinetics *b*, figure of merit (FOM) and acceptability factor are shown in Table 6.8. Good fit structures have FOM that is less than 3.5 % and a C_b that is less than 0.4 [62, 63]. The results in Table 6.8 show a good fit for all samples.

Table 6.8: Kinetic parameters determined from curve fitting for the main TL peaks of all the samples, the samples were irradiated to 40 Gy.

Sample	Activation energy E(eV^{-1})	Order of kinetics b	Effective frequency factor *s* (s^{-1})	FOM (%)	C_b
Unimplanted	0.97 ± 0.02	1.41 ± 0.06	2.39×10^8	3.8	0.34
1×10^{14}	0.91 ± 0.03	1.35 ± 0.60	2.49×10^8	3.1	0.34
5×10^{14}	0.96 ± 0.02	1.42 ± 0.10	5.13×10^7	2.9	0.34
1×10^{15}	0.91 ± 0.03	1.33 ± 0.13	3.74×10^9	3.6	0.36
5×10^{15}	0.91 ± 0.03	1.38 ± 0.26	1.47×10^9	3.3	0.35
1×10^{16}	0.91 ± 0.03	1.32 ± 0.08	2.96×10^9	3.6	0.36

The activation energy using the curve fitting was of the order of 0.92 ± 0.03 eV, with the order of kinetics as 1.4 and the frequency factor to be of the order $10^8\ s^{-1}$. These results are consistent with those obtained from Chen's peak shape and the whole glow methods.

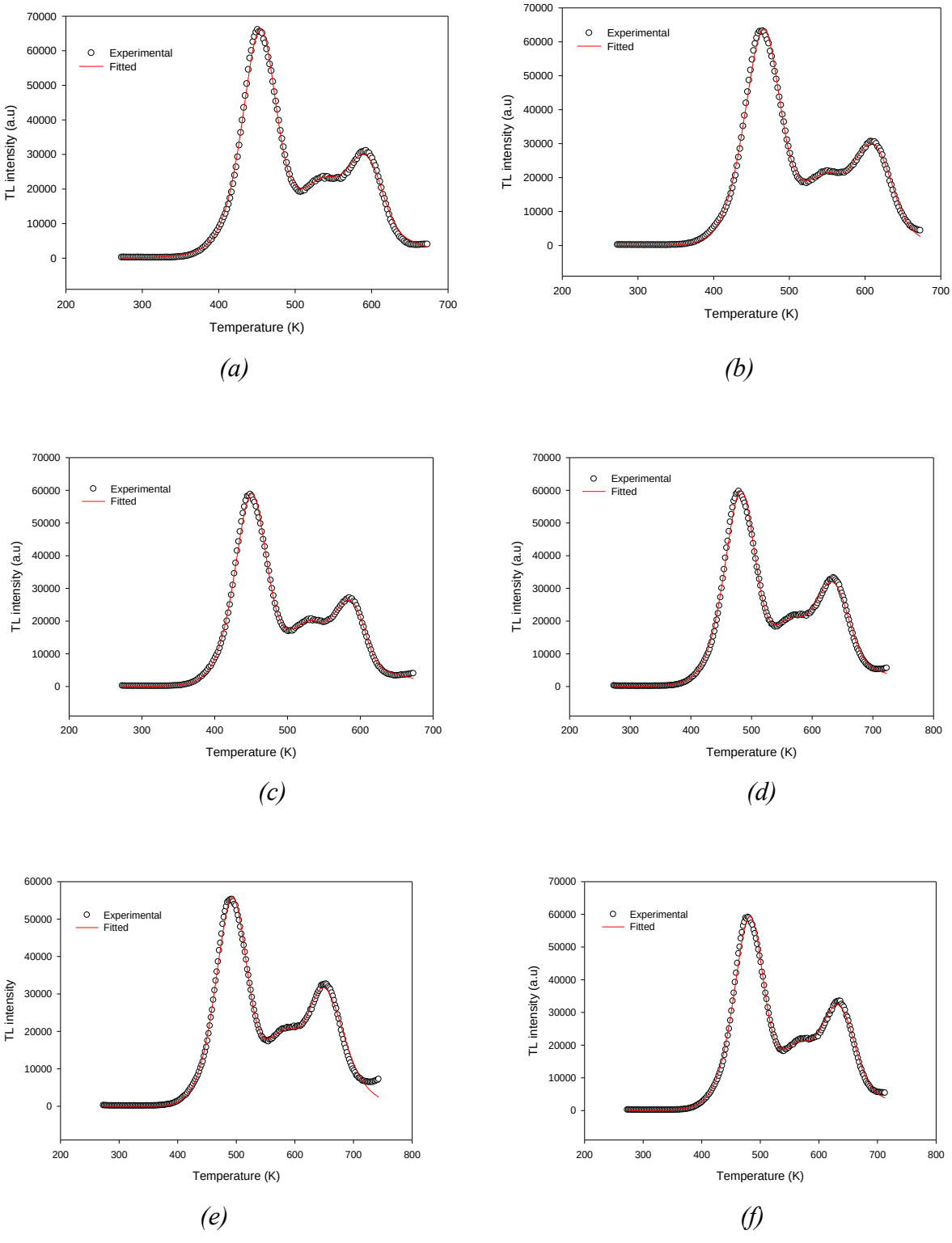

Figure 6.14: Results from curve fitting of the whole glow peak for the unimplanted sample (a) and implanted samples at fluences 1×10^{14} (b), 5×10^{14} (c), 1×10^{15}(d), 5×10^{15}(e), 1×10^{16} Ar^{+}/cm^{2}(f). All samples were irradiated with 40 Gy at a heating rate of 1 °C/s. Open circles are the experimental data and the solid line is the best fit calculated using equation (4.25).

6.2.2.6 Isothermal decay method

This method was also used to evaluate the kinetic parameters of the main thermoluminescence peak of unimplanted and implanted samples. The isothermal decay method involves irradiating a sample and quickly heating and holding it at a specific temperature T_i. Thermoluminescence is measured at that temperature for a certain time interval. For first order kinetics the luminescence intensity should decrease according to the exponential function

$$I = I_0 \exp\left(-sexp\left(-\frac{E}{kT_i)}\right)t\right). \tag{6.3}$$

A graph of $\ln(I)\ vs\ t$ will be linear with the slope of the line being m_i equal to $-\ sexp\left(\frac{E}{kT_i}\right)$. Taking the natural logarithm gives

$$\ln(|\text{slope}|) = \ln s - \frac{E}{kT_i} \tag{6.4}$$

Graphs of the $ln(slope)\ vs\ 1/kT$ should yield a straight line with slope -E and y-intercept equal to ln s [50].

Based on the peak temperatures of the main peak, isotherms in the range 150 – 170ºC were selected together with a time interval of 500 s. Isothermal decay curves of each sample were obtained by irradiating samples to 40 Gy and quickly heating and holding them at a temperature T_i for 500 s. The TL is then further measured to remove any residual signals. This process is repeated but using a different isotherm T_{i+1}

Figure 6.15 shows plots of $ln(slope)\ vs\ 1/kT$ used to evaluate the activation energy of the various samples. Table 6.9 shows the activation energy and frequency factor of the various samples using the isothermal method.

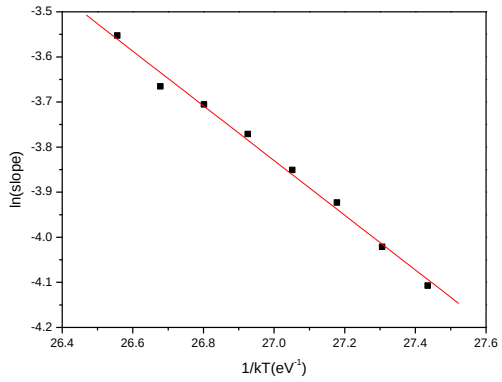

(a)

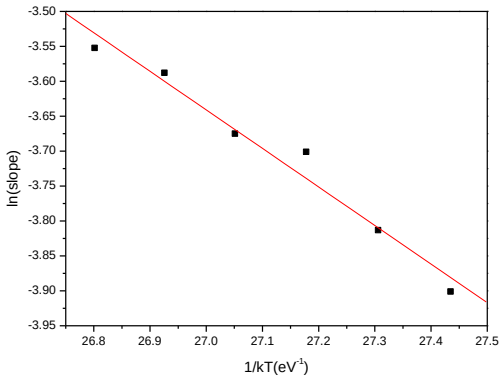

(b)

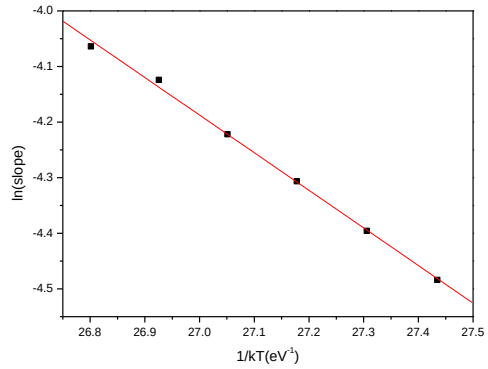

(c)

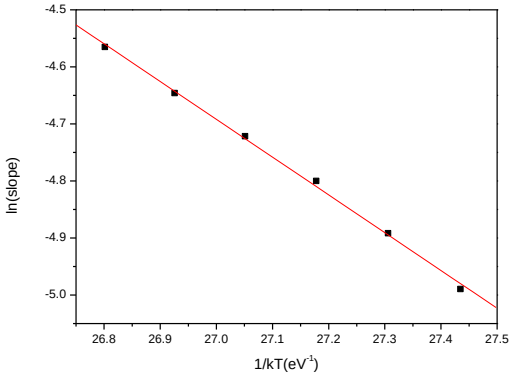

(d)

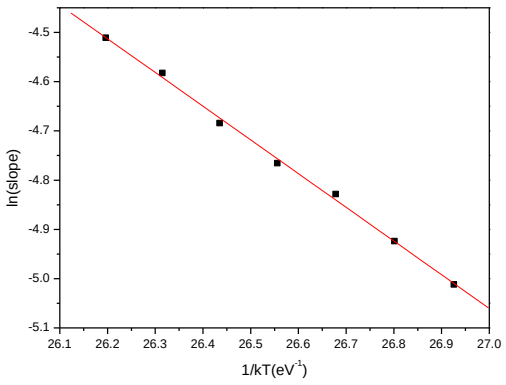

(e)

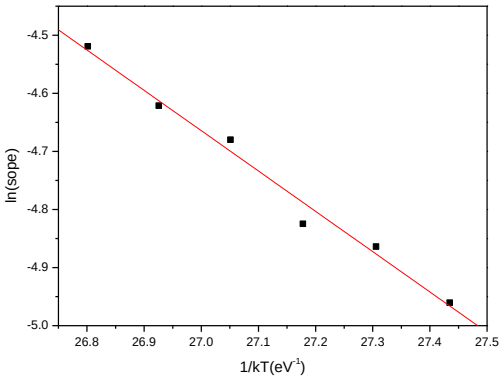

(f)

Figure 6.15: Plots of ln(slope) vs 1/kT used to determine the activation energy of the unimplanted (a) and implanted samples at fluences 1×10^{14} (b), 5×10^{14} (c), 1×10^{15} (d), 5×10^{15} (e) and 1×10^{16} Ar^{+}/cm^{2}(f).

Table 6.9: The activation energy and frequency factor of the unimplanted sample and implanted samples.

Sample	Activation energy E (eV)	Frequency factor s (s^{-1})
Unimplanted	0.61 ± 0.02	2.7×10^{5}
1×10^{14}	0.55 ± 0.04	7.7×10^{4}
5×10^{14}	0.68 ± 0.44	1.2×10^{6}
1×10^{15}	0.66 ± 0.01	5.3×10^{5}
5×10^{15}	0.68 ± 0.01	6.7×10^{5}
1×10^{16}	0.69 ± 0.04	1.3×10^{6}

The activation energy obtained using the isothermal method was about 0.65 ± 0.05 eV and the frequency factor was evaluated to be of the order $10^5\ s^{-1}$. This activation energy is lower than that obtained by using Chen's peak shape, whole Glow, and curve fitting methods this could be because of the choice of isotherms used. However, this method seems to be in good agreement with the Initial rise and various heating rate methods.

6.3 Dosimetric features

The thermoluminescence response of a material to irradiation dose is important in the field of medical physics and radiation protection. An ideal TL material should exhibit a linear dose response. However, several TL materials exhibit a non-linear dose response expressed by

$$I_{max} = aD^k \tag{6.5}$$

Where I_{max} is the maximum TL intensity, *D* is the dose and *a* and *k* are constants.
A log-log plot of $I_{max}\ vs\ D$ yields a straight line with slope *k*.
Halperin and Chen [64] studied the dose response of UV irradiated diamonds and found the slope *k* to be between 2 and 3. They termed this more than linear response superlinearity.
Chen and Mckeever [65] suggested the use of the term superlinearity in cases where the second derivative of the TL signal as a function of dose *S(D)* is greater than zero i.e., $d^2S/D^2>0$ and sublinear where $d^2S/D^2< 0$ and linear in cases where $d^2S/D^2=0$. They suggested a dimensionless quantity termed the superlinearity index *g(D)* expressed as

$$g(D) = \left[\frac{DS''(D)}{S'(D)}\right] + 1\ , \tag{6.6}$$

where *S'(D)* and *S''(D*) are the first and the second derivatives of *S(D).*

Values of g(D) >1 suggests superlinearity, *g(D)* =1 denotes a linear response and *g(D)*<1 indicates sublinearity.

However, it must be noted that knowledge of an analytical function which fits the experimental dose response curves is required for the application of equation (6.6)

6.3.1 Dose response of the main peak

The dose response of a TL material is of paramount importance for practical purposes. For an ideal TL dosimeter, the intensity of the light emitted is expected to be linearly related to the dose. In this study, the dose response from our samples was investigated by irradiating them with different doses from 40 to 200 Gy at a heating rate of 1°C/s. Figure 6.16 shows the influence of dose on the intensity and the superlinearity index of the main peak of the unimplanted sample. The inset shows that the peak temperature is independent of the dose.

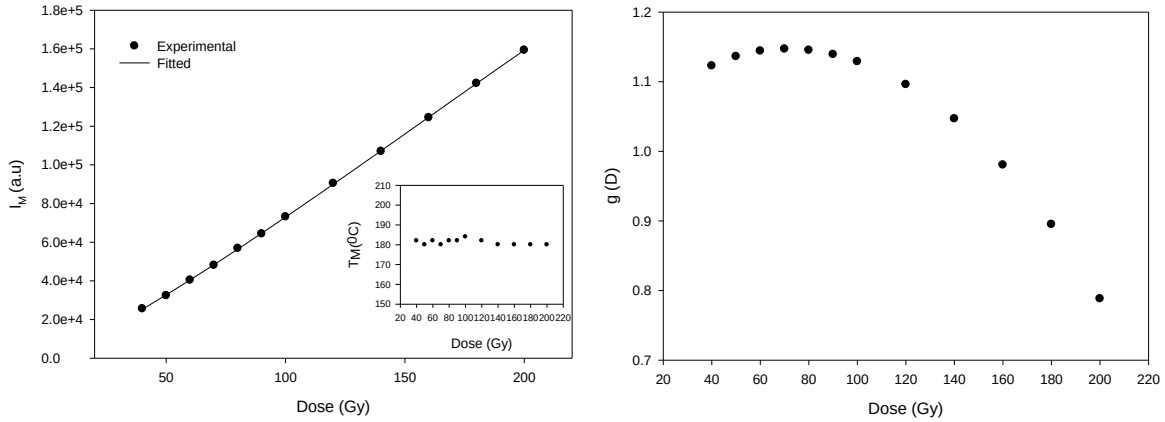

(a) *(b)*

Figure 6.16: The variation of peak intensity with dose with the inset showing a plot of peak temperature vs dose (a) and a plot of the superlinearity index g(D) vs dose D (b) for the unimplanted sample.

The dose response of the unimplanted sample can be described by the cubic function

$$S(D) = a + bD + cD^2 + dD^3 \,, \tag{6.7}$$

where $S(D)$ is the peak intensity for doses D between 40 Gy – 200 Gy and a, b, c, d are constants. A similar cubic function was used by Kalita and Chithambo to describe the dose response of Al_2O_3 doped with carbon and magnesium [66].

The graph of intensity as a function of dose shown in Figure 6.16 (a) was fitted using sigma plot package to obtain the parameters, a = 3316.77, b = 299.79 Gy^{-1}, c = 1.83 Gy^{-2}, d = - 0.0026 Gy^{-3}. The fit shown in Figure 6.16 (a) is represented by a solid line and the data points by filled circles. The cubic function is suitable to describe this dose response because it shows a best fit with an R^2 of 0.99. It should be noted that the dose response of all the samples was described by the cubic function (6.7), however different parameters were obtained.

The superlinearity index *g(D)* [64] was used to provide a quantitative description of the dose response for the main peak of the unimplanted sample and was evaluated using equation 6.6. *g(D)* describes how the slope of the dose response changes. A value of *g(D)* > 1 suggests superlinearity while a value of *g(D)* = 1 suggests a linear region and a *g(D)* < 1 denotes a sublinear region [64].

As shown in Figure 6.16 (b) g*(D)* > 1 for doses *D* in the range 40 to 140 Gy and therefore superlinear but sublinear in the range 160 Gy – 200 Gy where *g(D)* <1.

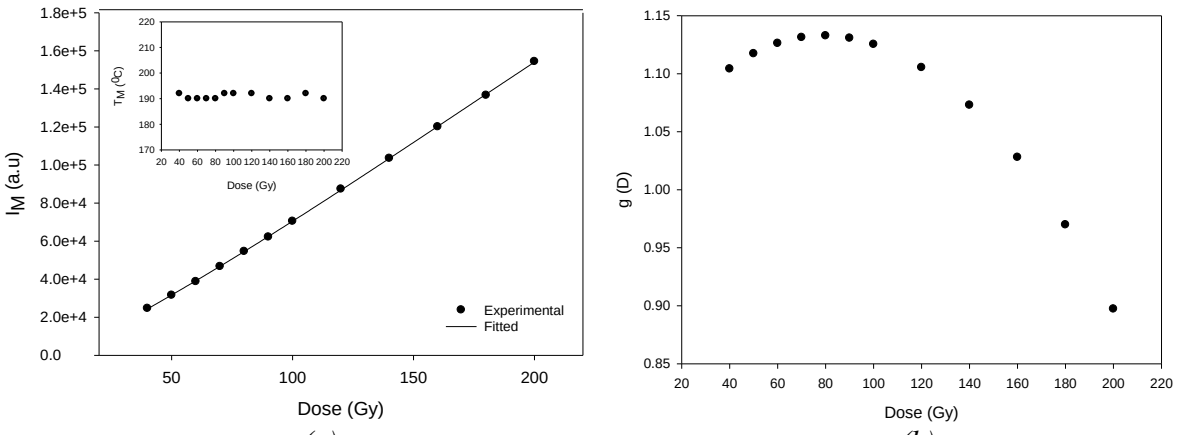

Figure 6.17: The variation of peak intensity with dose the inset showing a plot of peak temperature vs dose (a) and a plot of the super-linearity index g(D) vs dose D (b) for the sample implanted at 1×10^{14} Ar^{+}/cm^{2}.

The superlinearity index vs dose shown in Figure 6.17 (b) shows that *S(D)* is super-linear in the dose range from 40 – 160 Gy where *g(D)* > 1 and sublinear in the range 180 – 200 Gy where *g(D)* < 1 for the sample implanted at a fluence of $1\times10^{14}Ar^{+}/cm^{2}$.

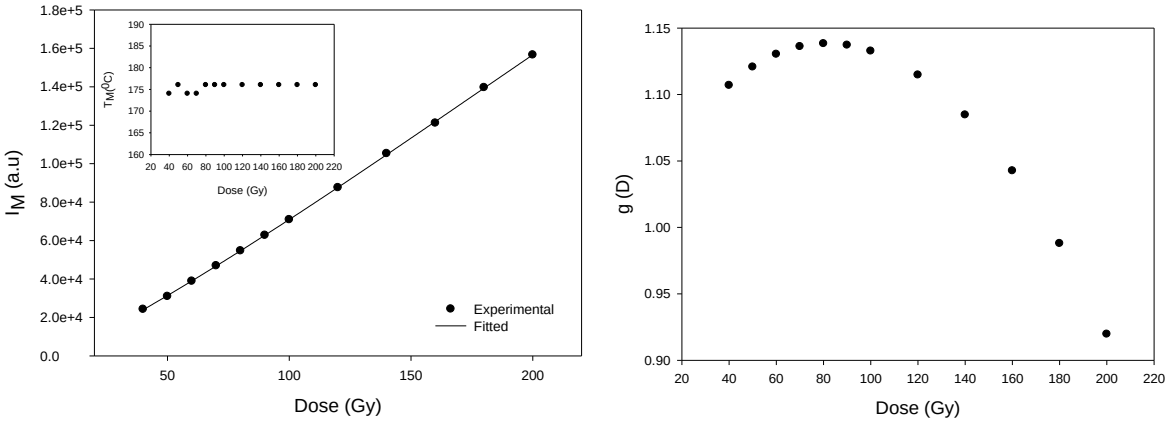

(a) *(b)*

Figure 6.18: The peak intensity as a function of dose with the inset showing the peak temperature as a function of dose (a)and the superlinearity as a function of dose (b) for the sample implanted at 5×10^{14} ions/cm^2. All measurements were carried out at a heating rate of 1ºC/s.

Figure 6.18 (b) shows that the dose response vs the superlinearity index *g(D)* described the dose to be superlinear *g(D)* > 1 for the range 40 – 160 Gy and then sublinear for the range 180 – 200 Gy for the sample implanted at 5×10^{14} Ar^+/cm^2.

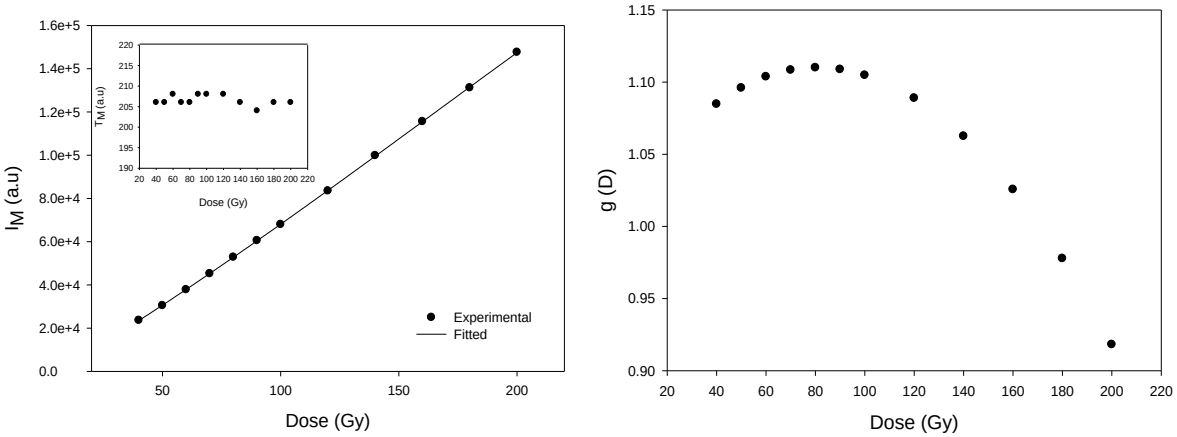

(a) *(b)*

Figure 6.19: The peak intensity as a function of dose with the inset showing the peak temperature as a function of dose (a)and the superlinearity as a function of dose (b) for the sample implanted at 1×10^{15} Ar^+/cm^2. All measurements carried out at a heating rate of 1 °C/s

Figure 6.19 (b) shows that the dose response vs the superlinearity index *g(D)* described the dose to be superlinear g(D) > 1 for the range 40 – 160 Gy and sublinear for the range 180 – 200 Gy for the sample implanted at a fluence of 1×10^{15} Ar^+/cm^2.

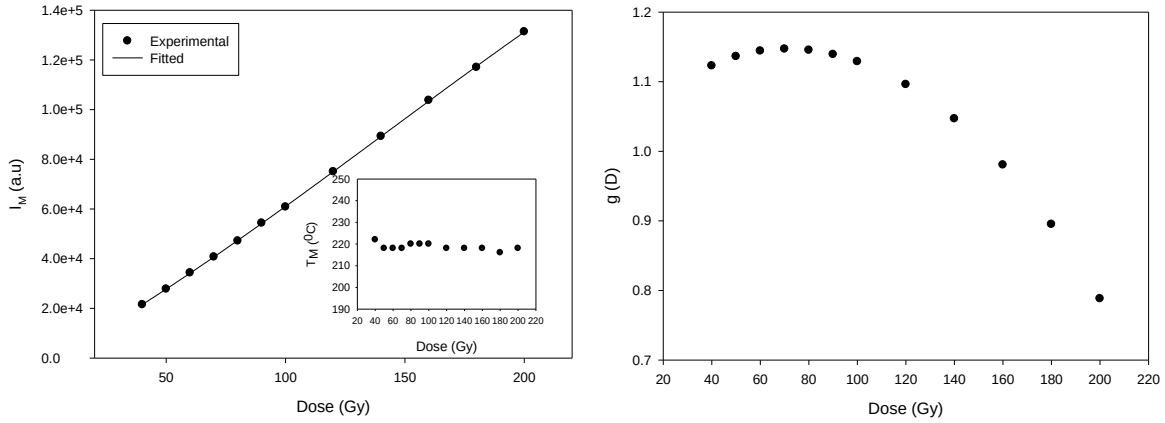

Figure 6.20: The peak intensity as a function of dose with the inset showing the peak temperature as a function of dose (a) and the superlinearity as a function of dose (b) for the sample implanted at 5 ×10^{15}Ar^{+}/cm^{2}. All measurements were carried out at a heating rate of 1°C/s.

Figure 6.20 (b) shows that the dose response vs the superlinearity index *g(D)* described the dose to be superlinear *g(D)* > 1 for the range 40 – 140 Gy and sublinear for the range 160 – 200 Gy for the sample implanted at 5 ×10^{15} Ar^{+}/cm^{2}.

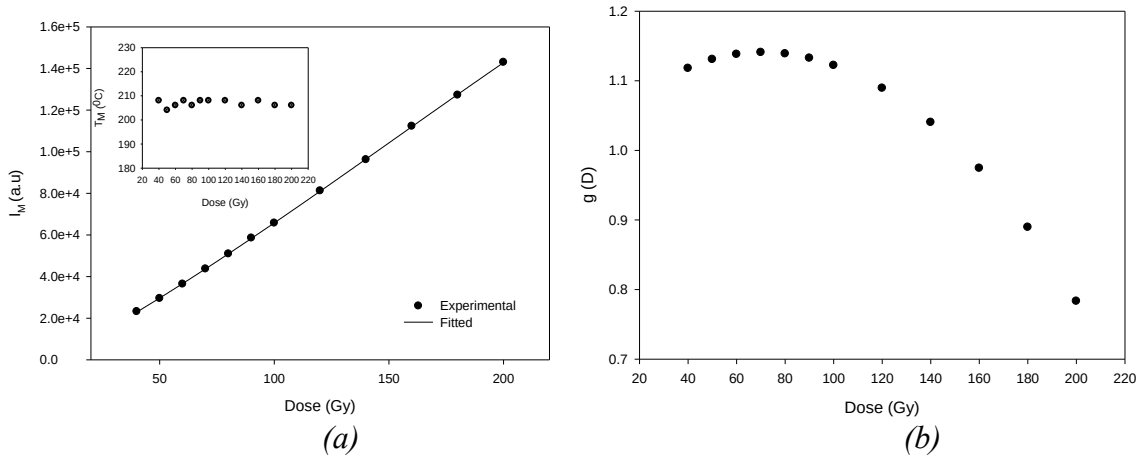

Figure 6.21: The peak intensity as a function of dose with the inset showing the peak temperature as a function of dose (a) and the superlinearity as a function of dose (b) for the sample implanted at 1×10^{16} Ar^{+}/cm^{2}. All measurements were carried out at a heating rate of 1 °C/s.

Figure 6.21 (b) shows that the dose response versus the superlinearity index *g(D)* described the dose to be superlinear *g(D)* > 1 in the range 40 – 140 Gy and sublinear in the range 160 – 200 Gy for the sample implanted at 1×10^{16} ions/cm^{2}.

6.4 Summary of the results on the kinetic analysis

The kinetic parameters obtained using the various techniques for all the samples are summarized in Table 6.10, Table 6.11

Table 6.10: Summary of the activation energies obtained using initial rise, peak shape, whole glow, curve fitting, various heating rate and isothermal methods

Sample	Initial rise *E* (eV)	Peak shape *E* (eV)	Whole glow *E* (eV)	Curve fitting *E* (eV)	VHR *E* (eV)	Isothermal *E* (eV)
Unimp	0.68 ± 0.01	1.12 ± 0.08	0.82 ± 0.02	0.97 ± 0.02	0.71 ± 0.06	0.61 ± 0.02
1×10^{14}	0.69 ± 0.01	1.06 ± 0.01	0.85 ± 0,02	0.91 ± 0.03	0.62 ± 0.04	0.55 ± 0.04
5×10^{14}	0.72 ± 0.11	1.18 ±0.04	0.78 ± 0.02	0.96 ± 0.02	0.72 ± 0.05	0.68 ± 0.44
1×10^{15}	0.73 ± 0.01	1.14 ± 0.05	0.84 ± 0.02	0.91 ± 0.03	0.52 ± 0.05	0.66 ± 0.01
5×10^{15}	0.75 ± 0.01	1.03 ± 0.14	0.87 ± 0.02	0.91 ± 0.03	0.49 ± 0.05	0.68 ± 0.01
1×10^{16}	0.72± 0.01	1.14 ± 0.05	0.84 ± 0.02	0.91 ± 0.03	0.52 ± 0.06	0.69 ± 0.04

Table 6.11: Summary of the frequency factors obtained using the whole glow, curve fitting, various heating rate and isothermal, initial rise and peak shape methods

Sample	Whole glow *s* (s^{-1})	Curve fitting *s* (s^{-1})	VHR s (s^{-1})	Isothermal *s* (s^{-1})	Initial rise *s* (s^{-1})	Peak shape *s* (s^{-1})
Unimp	2.0×10^{8}	2.4×10^{8}	2.5×10^{6}	2.7×10^{5}	1.5×10^{6}	2.3×10^{11}
1×10^{14}	3.0×10^{8}	2.5×10^{8}	1.7×10^{5}	7.7×10^{4}	1.3×106	2.2×10^{10}
5×10^{14}	9.2×10^{8}	5.1×10^{7}	5.0×10^{6}	1.2×10^{6}	5.0×10^{6}	1.2×10^{12}
1×10^{15}	1.0×10^{7}	3.7×10^{9}	0.1×10^{5}	5.3×10^{5}	1.6×10^{6}	5.4×10^{10}
5×10^{15}	1.4×10^{8}	1.5×10^{9}	0.2×10^{5}	6.7×10^{5}	1.9×10^{6}	2.1×10^{9}
1×10^{16}	9.5×10^{7}	3.0×10^{9}	0.1×10^{5}	1.3×10^{6}	1.4×10^{6}	7.0×10^{10}

Chapter 7

Conclusions

The thermoluminescence glow curves of Al_2O_3 samples both unimplanted and implanted at fluences of 1×10^{14}, 5×10^{14}, 1×10^{15}, 5×10^{15}, 1×10^{16} Ar^+/cm^2 were investigated. The samples were irradiated with 40 Gy at 1 °C/s unless otherwise stated. The TL glow curves of the samples displayed five distinct peaks with peak temperatures and intensities as denoted in Table 6.1. It was observed that the unimplanted sample showed the most intense thermoluminescence signal and that the intensity decreases with increasing fluence up to the highest fluence of 1×10^{16} Ar^+/cm^2 where a slight increase is observed. These results therefore show that argon ion implantation and fluence do not improve the thermoluminescence signal of Al_2O_3 samples. This suggests that non-radiative transition bands were formed following ion implantation leading to the reduction for the TL signal as observed by Nsengiyumva et al [60]. It might also be suggested that the creation of defect clusters and extended defects could be responsible for the reduction in TL signal following subsequent ion implantation and ion fluence increase. These results are contrary to previous studies conducted by Nsengiyumva et al in nitrogen implanted quartz [67] and argon implanted quartz [68] where the thermoluminescence signal was observed to increase with the implantation fluence.

Assessment of the order of kinetics using T_M-T_{STOP} and T_M-dose analysis showed that the peak temperatures T_M of the main peaks are independent of the T_{STOP} and dose. The main peak of both unimplanted and implanted samples was concluded to follow first order kinetics [50]. This was also reported by Nsengiyumva et al [60] for argon implanted Al_2O_3 and by Kalita et al for $\alpha AL_2O_3: C, Mg$ [66].

The kinetic parameters were evaluated using various methods and the results are summarized in Table 6.10 and Table 6.11. In general, the initial rise method yielded values of activation energy and frequency factor as E of 0.72 ± 0.02 eV and of the order $10^6 s^{-1}$. Chen's peaks shape method provided activation energies and frequency factor of the order $E_\tau = 1.15 \pm 0.08$ eV, $E_\delta = 1.08 \pm 0.04$ eV, $E_\omega = 1.11 \pm 0.06$ eV and $10^{10} s^{-1}$ respectively. The various

heating rate method gave values of the activation energy *E* and effective frequency factor *s* as 0.6 ± 0.1 eV and of the order $10^4 s^{-1}$ respectively. The peaks were determined to be affected by thermal quenching and the activation energy of thermal quenching *W* was evaluated to be 1.12 ± 0.20 eV. In their study of the kinetic analysis of the main peak of AL_2O_3C: Mg Kalita et al [66] obtained thermal quenching parameters *W* and *C* to be 0.99 ± 0.08 eV and of the order 10^{10} which is comparable to parameters obtained in this study. The whole glow peak gave values of *E* and *s* as 0.83 ± 0.03 eV and of the order $10^8 s^{-1}$ respectively, the order of kinetics was determined to be 0.9.

The curve fitting method evaluated *E*, *b* and *s* to be 0.92 ± 0.03 eV, 1.4 and of the order $10^8 s^{-1}$ respectively. The isothermal decay method determined the kinetic parameters *E* and *s* to be 0.65 ± 0.05 eV and of the order $10^5 s^{-1}$

It is worth noting that activation energy values obtained using IR, VHR and isothermal methods show some agreement and that the Chen's peak shape, whole glow peak curve and curve fitting methods are in good agreement with each other. The latter methods are more accurate as they employ the whole glow curve to evaluate trapping parameters. It is also worth noting that Nsengiyumva et al [60] obtained an activation energy of 1.00 eV and frequency factor of the order 10^{10} using WGP and curve fitting methods for argon ion implanted Al_2O_3. Kalita et al reported a value of activation energy ~ 1.36 eV and effective frequency of the order 10^{14} for αAL_2O_3: C, Mg [66] using the IR, peak shape WGP, curve fitting, VHR and phosphorescence methods. These values are similar to those evaluated in this study. Overall, the kinetic analysis carried out does not show any apparent trend with regards to ion implantation or fluence. This means that argon ion implantation did not affect the nature of electron traps.

For most dosimetric applications an ideal material should exhibit a linear dose response over a broad range of doses. The dose response of aluminum oxide samples in the range of 40 – 200 Gy was also investigated. It was observed that the dose response of samples can be described by the cubic function expressed by equation (6.7). The results obtained show that the unimplanted sample shows superlinearity in the range 40 – 140 Gy and sublinearity in the range 160 – 200 Gy. The sample implanted at 1×10^{14} ions/cm^2 shows superlinearity in the range 40 – 160 Gy and sublinearity in the range 180 – 200 Gy. The sample implanted at 5×10^{14} ions/cm^2 shows superlinearity in the range 40 – 160 Gy and sublinearity in the range 180 – 200

Gy. The sample implanted at 1×10^{15} ions/cm^2 shows superlinearity in the range 40 – 160 Gy and sublinearity in the range 180 – 200 Gy. The sample implanted at 5×10^{15} ions/cm^2 shows superlinearity in the range 40 – 140 Gy and sublinearity in the range 160 – 200 Gy. The sample implanted at the highest fluence, i.e, 1×10^{16} ions/cm^2 shows superlinearity in the range 40 – 140 Gy and sublinearity in the range 160 – 200 Gy. Overall, the dose response of the samples can be characterized by a more than linear response (superlinear) at doses less than 140 Gy and a sublinear dose response at doses higher than 160 Gy.

References

[1] Townsend, P., Chandler, P., & Zhang, L. (1994). Optical Effects of Ion Implantation (Cambridge Studies in Modern Optics). Cambridge: Cambridge University Press.

[2] Nastasi, M. and Mayer, J.W., 2006. Ion implantation and synthesis of materials. Springer, Verlag Berlin Heidelberg

[3] Mckeever, S.W.S., 1985. Thermoluminescence of Solids, Cambridge University Press. London New York.

[4] Chen and S.W.S. McKeever. Theory of Thermoluminescence and Related Phenomena. World Scientific Publishing, 1997.

[5] Bernas, H., & Nedellec, P. (Apr - 1 May 1981). Structural and electronic properties of ion implanted superconductors. Nuclear Instruments and Methods, 182/183(pt2), pp. 845-864

[6] Shannon, J., 1981. Shallow implanted layers in advanced silicon devices. Nuclear Instruments and Methods, 182, pp.545-552.

[7] Rubin, L. and Poate, J., 2003. Ion implantation in silicon technology. Industrial Physicist, 9(3), pp.12-15.

[8] Trinkaus, H., Singh, B.N. and Golubov, S.I., 2000. Progress in modelling the microstructural evolution in metals under cascade damage conditions. Journal of nuclear materials, 283 (2), pp.89-98.

[9] Picraux, S.T., 1984. Ion implantation in metals. Annual Review of Materials Science, 14(1), pp.335-372.

[10] McHargue, C.J., 1986. Ion implantation in metals and ceramics. International metals reviews, 31(1), pp.49-76.

[11] Dickson, K.E. 1985. The development of ion implantation technology in the UK semiconductor industry Physics in Technology, 16(4), pp.171-176.

[12] Rehn, L.E., Averback, R.S. and Okamoto, P.R., 1985. Fundamental aspects of ion beam surface modification: defect production and migration processes. Materia Science and Engineering, 69(1), pp.1-11.

[13] Dearnaley, G., 1983. The modification of materials by ion implantation. Physics in Technology, 14(5), pp.225-232.

[14] Bryant, F.J., 1982. Ion implantation and luminescence. Radiation Effects, 65(1-4) pp.81-93.

[15] Fink, D. and Chadderton, L.T., 2005. Ion-solid interaction: status and perspectives. Brazilian Journal of Physics, 35, pp.735-740.

[16] Sigmund, P., 2000. Stopping power: Wrong terminology. ICRU News, 2000, pp.5-7.

[17] Schou, J., 2007. Slowing-down processes, energy deposition, sputtering and desorption in ion and electron interactions with solids. by Daniel Brandt, Geneva, Switzerland, Vol. CERN-2007-003, pp.169-178.

[18] Khodyrev, V.A., Andrzejewski, R., Rivera, A., Boerma, D.O. and Prieto, J.E., 2011. Shower approach in the simulation of ion scattering from solids. Physical Review E, 83(5), pp.056707-056707.

[19] Williams, J.S., 1986. Materials modification with ion beams. Reports on Progress in Physics, 49(5), p.491.

[20] Marwick, A.D., 1989. Ion beam characterization and treatment. Metallurgical Transactions A, 20(12), pp.2627-2636.

[21] Nastasi, M., Michael, N., Mayer, J., Hirvonen, J.K. and James, M., 1996. Ion-solid interactions: fundamentals and applications. Cambridge University Press.

[22] Amekura, H., Voitsenya, V., Lay, T.T., Takeda, Y. and Kishimoto, N., 2001. X-ray

emission induced by 60 keV high-flux copper negative-ion implantation. Japanese Journal of Applied Physics, 40(2S), pp.1094-1096.

[23] Belykh, S.F., Evtukhov, R.N., Redina, I.V. and Ferleger, V.K., 1995. Ion-photon emission from metals implanted with ions of reactive elements. Nuclear Instruments and Methods in Physics Research Section B: Beam Interactions with Materials and Atoms, 95(3), pp.300-306.

[24] Xiao, Z., Cheng, G., Zhang, T. and Xu, F., 2000. Up-conversion luminescence from neodymium ion implantation silicon. Surface and Coatings Technology, 128, pp.461-464.

[25] Baragiola, R.A., Alonso, E.V. and Florio, A.O., 1979. Electron emission from clean metal surfaces induced by low-energy light ions. Physical Review B, 19(1), pp.121-129.

[26] Lindhard, J. and Scharff, M., 1961. Energy dissipation by ions in the keV region. Physical Review, 124(1), pp.128-130.

[27] Ziegler, J.F., Biersack, J.P. and Littmark, U.N.D.U., 1985. SRIM-The Stopping and Range of Ions in Solids. Pergamon. Press, New York.

[28] Bacon, D.J., Gao, F. and Osetsky, Y.N., 2000. The primary damage state in fcc, bcc and hcp metals as seen in molecular dynamics simulations. Journal of Nuclear Materials, 276(1-3), pp.1-12.

[29] Bringa, E.M., Wirth, B.D., Caturla, M.J., Stölken, J. and Kalantar, D., 2003. Metals far from equilibrium: From shocks to radiation damage. Nuclear Instruments and Methods in Physics Research Section B:, 202, pp.56-63.

[30] Watkins, G.D., 1977. Lattice vacancies and interstitials in silicon. Chinese Journal of Physics, 15(2), pp.92-101.

[31] Sood, D.K. and Dearnaley, G., 1975. Radiation damage in copper single

crystals. Journal of Vacuum Science and Technology, 12(1), pp.463-467.

[32] Sharkeev, Y.P., Kozlov, E.V., Didenko, A.N., Kolupaeva, S.N. and Vihor, N.A., 1996. The mechanisms of the long-range effect in metals and alloys by ion implantation. Surface and Coatings Technology, 83(1-3), pp.15-21.

[33] Friedland, E., Van der Berg, N.G., Meyer, O. and Kalbitzer, S., 1996. Study of implantation damage ranges in metals at temperatures ranging from 5 to 300 K. Nuclear Instruments and Methods in Physics Research Section B:, 118(1-4), pp.29-33.

[34] Ali, M.O., 1993. Elementary solid-state physics: principles and applications. Addison-Wesley publishing company.

[35] Bolse, W., 1994. Ion-beam induced atomic transport through bi-layer interfaces of low- and medium-Z metals and their nitrides. Materials Science and Engineering: R: Reports, 12(2), pp.7-121.

[36] Jiménez-Sáez, J.C., Domínguez-Vázquez, J., Pérez-Martín, A.M.C. and Jiménez-Rodríguez, J.J., 2002. Simulation of ion beam induced atomic mixing of interfaces. Vacuum, 67(3-4), pp.635-639.

[37] De La Rubia, T.D. and Guinan, M.W., 1991. New mechanism of defect production in metals: A molecular-dynamics study of interstitial-dislocation-loop formation in high-energy displacement cascades. Physical review letters, 66(21), pp.2766-2769.

[38] Saarinen, K., Hautojärvi, P., Keinonen, J., Rauhala, E., Räisänen, J. and Corbel, C., 1991. Defect structure and recovery in hydrogen-implanted semi-insulating GaAs. Physical Review B, 43(5), pp.4249-4262.

[39] Bacon, D.J. and de la Rubia, T.D., 1994. Molecular dynamics computer simulations of displacement cascades in metals. Journal of Nuclear Materials, 216, pp.275-290.

[40] Heinisch, H.L., Singh, B.N. and de la Rubia, T.D., 1994. Calibrating a multi-model approach to defect production in high energy collision cascades. Journal of nuclear materials, 212, pp.127-131.

[41] Chen, R. and Pagonis, V., 2011. Thermally and optically stimulated luminescence: a simulation approach. John Wiley & Sons.

[42] Wick, F.G., 1927. The effect of X-rays upon thermoluminescence. JOSA, 14(1), pp.33-44.

[43] Daniels, F., Boyd, C.A. and Saunders, D.F., 1953. Thermoluminescence as a research tool. Science, 117(3040), pp.343-349.

[44] Bos, A.J., 2017. Thermoluminescence as a research tool to investigate luminescence mechanisms. Materials, 10(12), pp.1357-1379.

[45] Randall, J.T. and Wilkins, M.H.F., 1945. The phosphorescence of various solids. Proceedings of the Royal Society of London. Series A. Mathematical and Physical Sciences, 184(999), pp.347-364.

[46] Randall, J.T. and Wilkins, M.H.F., 1945. Phosphorescence and electron traps-I. The study of trap distributions. Proceedings of the Royal Society of London. Series A. Mathematical and Physical Sciences, 184(999), pp.365-389.

[47] Randall, J.T. and Wilkins, M.H.F., 1945. Phosphorescence and electron traps II. The interpretation of long-period phosphorescence. Proceedings of the Royal Society of London. Series A. Mathematical and Physical Sciences, 184(999), pp.390-407.

[48] Garlick, G.F.J. and Gibson, A.F., 1948. The electron trap mechanism of luminescence in sulphide and silicate phosphors. Proceedings of the Physical Society (1926-1948), 60(6), pp.574-590.

[49] May, C.E. and Partridge, J.A., 1964. Thermoluminescent kinetics of alpha-irradiated alkali halides. The Journal of Chemical Physics, 40(5), pp.1401-1409.

[50] Pagonis, V., Kitis, G. and Furetta, C., 2006. Numerical and practical exercises in thermoluminescence. Springer Science & Business Media.

[51] Kivits, P. and Hagebeuk, H.J.L., 1977. Evaluation of the model for thermally stimulated luminescence and conductivity; reliability of trap depth determinations. Journal of Luminescence, 15(1), pp.1-27.

.

[52] Chen, R., 1969. On the calculation of activation energies and frequency factors from glow curves. Journal of Applied Physics, 40(2), pp.570-585.

[53] Halperin, A. and Braner, A.A., 1960. Evaluation of thermal activation energies from glow curves. Physical Review, 117(2), pp.408-415

[54] Porfianovitch, I.A., 1954. Expressions for Evaluating the Kinetic Parameters. Exp. J. Theor. Phys. USSR, 26, pp.696-702.

[55] Booth, A.H., 1954. Calculation of electron trap depths from thermoluminescence maxima. Canadian Journal of Chemistry, 32(2), pp.214-215.

[56] Kitis, G., Gomez-Ros, J.M. and Tuyn, J.W.N., 1998. Thermoluminescence glow-curve deconvolution functions for first, second and general orders of kinetics. Journal of Physics D: Applied Physics, 31(19), pp.2636-2641.

[57] Horowitz, Y.S. and Yossian, D., 1995. Computerised glow curve deconvolution: application to thermoluminescence dosimetry. Radiation Protection Dosimetry, 60(1), pp.3-3.

[58] RISØ, T. and Manual, O.U., 2010. Guide to “The Risø TL/OSL Reader”. RISØ DTU. Denmark .

[59] Akselrod, M.S., Kortov, V.S., Kravetsky, D.J., Gotlib, V.I., 1990. Radiat. Prot. Dosim. 32, pp 15-20

[60] Nsengiyumva, S., Chithambo, M.L., Topic, M. and Pichon, L., 2019.Thermoluminescence and fluorescence studies of argon-implanted aluminium oxide. Radiation Effects and Defects in Solids, 174(7-8), pp.708-720.

[61] Pagonis, V., Blohm, L., Brengle, M., Mayonado, G. and Woglam, P., 2013. Anomalous heating rate effect in thermoluminescence intensity using a simplified semi-localized transition (SLT) model. Radiation Measurements, 51, pp.40-47.

[62] Balain,H.G and Eddy, N.W., 1997. Figure-of-merit (FOM), an improved criterion over the normalized chi-squared test for assessing goodness-of-fit of gamma-ray spectral peaks. Nuclear Instruments and Methods, 145(2), pp.389-395

[63] Kitis, B., 2001. TL glow-curve deconvolution functions for various kinetic orders and continuous trap distribution: Acceptance criteria for E and s values. Journal of Radioanalytical and Nuclear Chemistry, 247(3), pp.697-703.

[64] Halperin, A. and Chen, R., 1966.Thermoluminescenceof semiconducting diamonds. Physical Review,148(2), pp.839-843

[65] Chen, R. and McKeever, S.W.S., 1994. Characterization of nonlinearities in the dose dependence of thermoluminescence. Radiation Measurements, 23(4), pp.667-673.

[66] Kalita, J.M. and Chithambo, M.L., 2017. The influence of dose on the kinetic parameters and dosimetric features of the main thermoluminescence glow peak in α-Al2O3: C, Mg. Nuclear Instruments and Methods in Physics Research Section B, 394, pp.12-19

[67] Nsengiyumva, S., Chithambo, M.L. and Pichon, L., 2015. Influence of nitrogen implantation on thermoluminescence of synthetic quartz. Radiation Effects and Defects in Solids, 170(1), pp.18-29.

[68] Nsengiyumva, S., Chithambo, M.L. and Pichon, L., 2016. Influence of argon-implantation on conventional and phototransferred thermoluminescence of synthetic quartz. Radiation Effects and Defects in Solids, 171(3-4), pp.328-339.